

HIGH-RESOLUTION LARGE-EDDY SIMULATIONS OF FLOW IN A STEEP ALPINE VALLEY. PART II: FLOW STRUCTURE AND HEAT BUDGETS

Andreas P. Weigel^{1*}, Fotini K. Chow², Mathias W. Rotach^{1,3},
Robert L. Street² and Ming Xue⁴

¹Institute for Atmospheric and Climate Science, ETH, Zürich, Switzerland

²Environmental Fluid Mechanics Laboratory,
Stanford University, Stanford, CA, USA

³Swiss Federal Office for Meteorology and Climatology,
MeteoSwiss, Zürich, Switzerland

⁴School of Meteorology and Center for Analysis and Prediction of Storms,
University of Oklahoma, USA

**Corresponding author:* Andreas Weigel, MeteoSwiss, Krähbühlstrasse 58, P.O. Box 514, CH-8044 Zürich, Switzerland. Email: andreas.weigel@meteoswiss.ch

Abstract

This paper analyzes the three-dimensional flow structure and the heat budget in a typical medium-sized and steep Alpine valley, the Riviera Valley in southern Switzerland. Aircraft measurements from the MAP-Riviera field campaign reveal a very pronounced valley-wind system, including a strong curvature-induced secondary circulation in the southern valley entrance region. Accompanying radio soundings show that the growth of a well-mixed layer is suppressed, even under convective conditions. Our analyses are based on the MAP-Riviera measurement data and the output of high-resolution large-eddy simulations using the Advanced Regional Prediction System (ARPS). Three sunny days of the measurement campaign are simulated. Using horizontal grid-resolutions of 350 m and 150 m (with a vertical resolution as fine as 20 m), the model reproduces the observed flow features very well. The ARPS output data are then used to calculate the components of the heat budget of the valley atmosphere, first in profiles over the valley base, then as averages over almost the entire valley volume. The analysis shows that the suppressed growth of the well-mixed layer is due to the combined effect of cold-air advection in the along-valley direction and subsidence of warm air from the free atmosphere aloft. It is further influenced by the local cross-valley circulation. This had already been hypothesized on the basis of measurement data, and is now confirmed through a numerical model. Averaged over the entire valley, subsidence turns out to be one of the main heating sources of the valley atmosphere and is of comparable magnitude to turbulent heat flux divergence. On the mornings of two out of the three simulation days, this subsidence is even identified as the only major heating source and thus appears to be an important driving mechanism for the onset of thermally driven up-valley winds.

1. Introduction

On fair-weather days, complicated thermally-driven flow patterns can develop in mountain valleys and affect the atmospheric boundary layer evolution. Such flow patterns are typically a superposition of several scales of motion, including local *slope winds* (directed normal to the valley axis and along the slopes), channeled and thermally-induced *valley winds* (parallel to the valley axis) as well as mountain-plain winds on the regional scale. The phenomenology of these flows has been well investigated and is comprehensively described in numerous reviews (e.g. Wagner 1938; Barry 1992; Whiteman 1990, 2000). Slope winds are understood to arise as a consequence of horizontal density gradients between the surface layer over the slopes and the air over the center of the valley. Their physics can be reproduced by relatively simple conceptual models (Egger 1990). As far as valley winds are concerned, however, there is still some controversy regarding the driving mechanisms. This paper uses large-eddy simulation of flow in a steep, Alpine valley to investigate the nature of along-valley wind formation using the heat budget as an analysis tool.

It is known that the diurnal cycle of potential temperature in a valley atmosphere reveals a higher amplitude than the corresponding cycle over an adjacent plain (e.g. Neiningner 1982; Vergeiner and Dreiseitl 1987). While it is plausible that the resulting gradients in hydrostatic pressure drive winds in the along-valley direction, it is not yet clear why valleys heat more during the day and cool more at night than adjacent plains. Often, this is explained by means of the simple TAF (topographic amplification factor) concept (e.g. Wagner 1938; Steinacker 1984; McKee and O'Neil 1989). It is based on a volume argument, stating that (in the daytime case) a given amount of incoming solar radiation applied over a mountain valley heats a smaller volume of air than if applied over a plain, resulting in a larger heating rate of the valley atmosphere. Analogously, the nocturnal cooling rate (driven by the emission of longwave radiation

from the surface) is stronger in a valley than over flat terrain. The main limitation of the TAF concept is its assumption that the control volume must be thermodynamically closed, i.e. that no heat must be exchanged with the synoptic-scale flow in the free atmosphere above the valley. Moreover, it fails in the case of rectangular valleys. Another concept, which has been developed on the basis of idealized simulations, suggests subsidence heating as an important driving mechanism (Rampanelli et al. 2004): due to a thermally induced cross-valley circulation, which extends well above the valley top, warm air of the free atmosphere is forced to subside, thus warming the valley. So far, however, there have been very few estimates of the heat budget terms in a daytime valley atmosphere from measurements (e.g Hennemuth 1987; Kalthoff et al. 2000; Weigel and Rotach 2004), and they lack the spatial and temporal resolution to quantitatively assess the underlying heating mechanisms.

With the advances of computer technology, high-resolution numerical simulations have become an important tool in the investigation of small-scale processes and the flow structure over mountainous terrain (e.g. De Wekker et al. 2005; Gohm et al. 2004; Zängl et al. 2004, to mention only very recent studies). Such simulations can be used for heat budget analyses. Fast et al. (1996), for example, used the Regional Atmospheric Prediction System (RAMS, Pielke et al. 1992) to investigate the night time heat budget of the Sindbad Basin in Colorado and were able to partly confirm the measurements of Whiteman et al. (1996).

We have chosen the Riviera Valley in southern Switzerland (base width: 1.5 km, length: 15 km, depth: 2-2.5 km) to investigate the daytime flow structure, thermal characteristics and, ultimately, the heat budget in a typical medium-sized alpine valley. In our approach, we combine measurements from the MAP-Riviera field campaign (Rotach et al. 2004) with the output of high-resolution large-eddy simulations (LES). For the modeling, we use the Advanced Regional Prediction System (ARPS, Xue et al. 2000, 2001, 2003). In Part I of this work (Chow et al. 2005), an optimal model setup

for simulating flow in the Riviera Valley with ARPS is described and results for one of the three days are evaluated by means of comparisons to radiosonde and surface data. Here, we use this setup to simulate and analyze three days of the measurement campaign (21, 22 and 25 August 1999) with fair-weather conditions. The experimental and numerical context is briefly described in the next section. Section 3 characterizes the three-dimensional flow structure in the valley and compares model results with aircraft measurements. The thermal structure is elaborated in Section 4, including a heat budget analysis of profiles over the valley base. Finally, the heat budget of the entire valley is analyzed in Section 5, and put into the context of the TAF and subsidence concepts of valley warming.

2. The field experiment and numerical simulations

The experimental setup of the MAP-Riviera Project has been extensively described by Rotach et al. (2004). The dataset obtained during the measurement campaign includes radio soundings and sonic and profile measurements, among others, at various surface stations. A light research aircraft (Neininger et al. 2001) was also employed. Focusing on both the mean and turbulence structures, the dataset is of unprecedented completeness with respect to boundary layer studies in such complex topography. In Part I (Chow et al. 2005), radiosonde and surface measurements are used to quantitatively evaluate the performance of ARPS in the Riviera Valley for the August 25 case. Here we focus primarily on the assessment of the three-dimensional flow-structure in the daytime Riviera atmosphere. The model performance in this aspect can be qualitatively evaluated by means of the airborne measurements (Weigel and Rotach 2004).

Chow et al. (2005) have described the numerical context for the simulation of the Riviera atmosphere in detail. Simulations were quantitatively evaluated for 25 August 1999, as data quality and synoptic conditions were most 'ideal' on this day. The setup

which has proven to yield the best results for 25 August is the so-called “LU-SM”-setup (Chow et al. 2005). In this setup, ARPS is run in a one-way nesting mode. A grid of 9 km horizontal resolution is initialized from ECMWF analysis data and then successively nested down to grids of finer horizontal resolutions (3 km, 1 km, 350 m and 150 m). All simulations start at 1800 UTC of the previous day (local daylight saving time = UTC + 2 hours).

The best setup for the simulation of 21 and 22 August has turned out to be almost identical to the “LU-SM” setup. The only major difference is that on 21 and 22 August the model fields of the first nesting level (9 km resolution) are additionally nudged over the entire simulation period to the respective interpolated ECMWF fields, yielding some further improvement of the model output. This step has been necessary due to the more complicated synoptic conditions on 21 and 22 August: while 25 August was almost entirely cloud-free in all nesting-domains, the Alps were partially cloud-covered on 21 and 22 August. On 20 August - the day of initialization for the simulation of 21 August - there is even rainfall over the larger part of the Swiss Alps, making the model-initialization particularly error-prone and the nudging process important.

Unless otherwise stated, data from model runs on the 350 m grid (finest vertical resolution of 30 m) are used in this paper, as the 350 m grid is the finest domain still containing the entire Riviera Valley. The 150 m grid (finest vertical resolution of 20 m) which does not cover the whole valley, has been used in Section 4b, where profiles of heat budget components over the narrow valley floor are assessed. The two high-resolution domains (350 m and 150 m) are shown in Fig. 1.

Regarding the choice of initial soil moisture distribution - one of the most sensitive parameters - the “LU-SM”-setup of Chow et al. (2005) has proven to give the best results as before. Following this setup, ECMWF soil moisture values are used on the 9 km and 3 km grids, a semi-empirical three-level initialization on the 1 km grid, and

output data of the Water Flow and Balance Simulation Model (WaSiM-ETH, Jasper 2001) for the ARPS runs on the 350 m and 150 m grids. For the three-level soil moisture initialization of the 1 km grid, the same values are used as on 25 August (see Table 3 in Chow et al. 2005).

In Fig. 2, the diurnal cycle of measured and simulated surface winds and potential temperatures at measurement site A1 (Bosco di Sotto, see Fig. 1) are displayed for 21 and 22 August (for 25 August see Figs. 4 and 5 in Chow et al. 2005). Table 1 shows the corresponding root-mean-square-errors (rmse) and mean errors (bias) for comparisons of the modeled surface wind speed, wind direction and potential temperature to the measurements. Bias and rmse are calculated in the same manner as described by Chow et al. (2005). The ARPS data used in these comparisons are extracted from the lowest model level (i.e. 15 m a.g.l.), while the observational data are averages of measurements at 15.9 m and 28 m a.g.l. The measurement level at 28 m has been included because the lower level (15.9 m) is partially influenced by surface layer effects from the plant canopy which are not captured in the model. On both days the diurnal cycles of potential temperature and surface winds are well reproduced by the model. On 21 August, however, the surface valley-wind magnitude is generally too large (on average by about 2.5 m s^{-1}), and simulated night-time surface temperatures are about 3-4 °C too warm. This warm bias is due to a shallow nocturnal ground inversion, which is observed from the radiosonde measurements (not shown) but not reproduced by the model. A reason for this model failure may be that the near-surface valley winds are overestimated by the model in the first place, thus producing too much vertical mixing on the surface. The skill scores of these simulations at surface site A1 are listed in Table 1. It can be seen that the rmse and bias of wind speed and particularly potential temperature are better on 22 August than on 21 August. We believe that this is due to the difficult initialization situation on 20 August, as mentioned above. Compared to other recent modeling studies over terrain of similar complexity (e.g. Zängl et al.

2004), the bias and rmse of 21 August are still of comparable if not better quality. Moreover, in this paper our focus is on the daytime atmosphere, where the errors are lower than the 24-hour-averages given in Table 1.

In Fig. 3, modeled vertical profiles of potential temperature are compared to radiosondes launched at site A1. A comparison of wind profiles is not possible due to a failure in the measurements. The skill scores have been calculated using data up to an altitude of 6 km (see Table 2). Again, 21 August shows a worse average rmse than 22 August, namely 1.23 K vs. 0.85 K, but this is still considered low. Given the more complicated synoptic conditions on 21 and 22 August, the results are surprisingly good and justify the use of the ‘LU-SM’-setup from 25 August on 21 and 22 August, at least for the evaluation of the daytime atmosphere. While the model fails to reproduce the mid-level inversions mostly seen between 3 and 4 km altitude, this shortcoming does not influence the following analyses, as this paper focuses on processes occurring within the valley atmosphere, i.e. at altitudes lower than 3 km.

3. Flow patterns of the valley atmosphere

Weigel and Rotach (2004) identified several unexpected features in the three-dimensional flow structure of the Riviera Valley from the MAP-Riviera observations, particularly from the aircraft measurements. Here, we describe the flow structure as obtained from ARPS and compare the results to these measurements.

a. Valley-wind structure

The modeled and measured time-series of surface winds at station A1 (21 and 22 August in Fig. 2; 25 August in Chow et al. 2005, Fig. 4)) show a pronounced valley-wind system with weak nocturnal down-valley flows (about 330°) and stronger up-

valley winds (about 150°) during the day, a pattern which is typical for thermally driven valley winds. Moreover, the simulations reveal potential temperature gradients in the along-valley direction of the Riviera Valley system (not shown), supporting the notion that the valley winds are of thermal origin. Aircraft observations show that the three-dimensional structure of the up-valley winds has a very distinct shape: in the southern half of the valley, the up-valley wind-speed has its maximum next to the west-facing slope, while further north the up-valley flow is uniformly spread over the valley diameter (Weigel and Rotach 2004). This pattern is well-reproduced by the model, as demonstrated for 21 August in Fig. 4, which shows the modeled afternoon wind-vectors from a bird's-eye view at an altitude of 900 m asl and the corresponding airborne observations. Simulations and measurements of 22 and 25 August reveal the same flow pattern (not shown).

A vertical cross-section through the asymmetric valley flow in a slice approximately 3.5 km north of the southern valley mouth shows a jet-like flow structure with a distinct wind speed maximum on the order of 10 m s^{-1} , both in the airborne measurements and the simulations (Fig. 5). Weigel and Rotach (2004) attribute this behavior to centrifugal forces: the air coming from the Magadino Valley in the southwest has to flow around a sharp bend at the town of Bellinzona to enter the Riviera Valley (see Fig. 1a). Due to its inertia the air is pushed towards the west-facing slope. Similar behavior has also been observed in other curved valleys such as the Wipp Valley in Austria (e.g. Fig. 16 in Gohm et al. 2004).

b. *Cross-valley circulations*

In the 'classical' textbook picture (Whiteman et al. 2000), the atmosphere in a sun-lit valley is expected to develop a symmetric double-circulation with air rising along the heated slopes and subsiding in the valley center. In the case of significant temperature

differences between the two valley side-walls, this circulation structure transitions to a simple cross-valley circulation with air rising along the warmer side and subsiding next to the colder side. Fig. 6 shows the simulated cross-valley flow in two slices through the valley on 22 August: one in the northern part of the valley, and one close to the southern valley entrance (at the positions of slices ‘S150’ and ‘N150’ in Figure 1b). At 0830 UTC, both cross-sections show a shallow layer of up-slope flow next to the east-facing slope, which is sun-exposed at that time. The rest of the valley atmosphere is characterized by slow subsidence (on the order of 0.3 m s^{-1}). Two hours later, when both slopes are exposed to direct shortwave solar radiation, the west-facing wall also develops a slope wind layer (not shown). The model output is thus consistent with the ‘classical’ picture of a symmetric double-circulation. Confirmation with aircraft data, however, is not possible, as the slow subsidence motion is beyond measurement accuracy.

At 1230 UTC the situation changes significantly: the two slices reveal very pronounced circulation patterns of different type. The cross-valley circulation rotates in the counter-clockwise sense in the northern cross-section, and in the clockwise sense in the southern valley entrance region. At this time, the west-facing side is already more sun-exposed than the east-facing slope (Matzinger et al. 2003), meaning that the counter-clockwise circulation pattern of Fig. 6(c) is the expected thermally driven flow, with air rising along the heated west-facing slope and subsiding on the cooler east-facing side. Interestingly, the situation at the southern slice is reversed, with a strong downward motion on the sun-exposed slope. Fig. 7 shows that this surprising phenomenon of an ‘anti-thermal’ clockwise circulation in the southern valley entrance region is also found on 21 August and 25 August, but on the latter two days a shallow layer of up-slope flow persists on the west-facing wall next to the subsiding air. On all three days, the ‘anti-thermal’ circulation is very pronounced with vertical velocity magnitudes on the order of $0.5 - 1 \text{ m s}^{-1}$. Weigel and Rotach (2004) have also identi-

fied this structure in the aircraft measurements. They attribute it to the sharp curvature of the streamlines in the valley entrance region, where the up-valley winds flow around a sharp bend to enter the Riviera Valley (see Fig. 1a). As is known from curved flows of channeled water (e.g. Rozovskii 1957; Kalkwijk and Booij 1986; Geyer 1993), and as described by Weigel and Rotach (2004), curvature induces a ‘secondary circulation’ due to local imbalances between counteracting pressure-gradient and centrifugal forces. In the Riviera Valley, the secondary circulation is apparently strong enough to dominate over a counter-clockwise thermally driven circulation which would develop otherwise. The observed coexistence of two distinct and opposed circulation patterns within one valley is schematically summarized in Figure 8. A full quantitative evaluation of the momentum budget within these two circulation schemes is intended for a future paper.

4. Temperature structure

a. Profiles of potential temperature over the valley floor

The diurnal evolution of temperature profiles in the Riviera Valley is different from what is typically expected in a convectively forced boundary layer (Weigel and Rotach 2004). The growth of the well-mixed layer has been observed to consistently cease by noon; sometimes, the valley atmosphere even stabilizes almost down to the valley floor despite positive surface heat fluxes. This is, for example, the case in the profiles of Figs. 3(c) and (e) - both in the measurements and the simulations. The difference between the atmosphere in the Riviera Valley and a ‘normal’ convective boundary layer becomes particularly apparent in Fig. 9, where time-height plots of modeled gradients of potential temperature on 25 August are shown for soundings in the Riviera Valley and at a location approximately 50 km southwest of the Riviera Val-

ley, i.e. at the beginning of the foothills of the Alps (data obtained from the 1 km grid). While the well-mixed layer stops growing in the Riviera Valley by noon (10 UTC) and then continuously shrinks, outside the Alps it keeps growing until about 1500 UTC, becoming almost three times as deep as in the Riviera Valley.

Kuwagata and Kimura (1995, 1997) measured and simulated similar behavior in the Ina Valley, Japan, and Rampanelli et al. (2004) observed the same phenomenon in their idealized simulations. In both studies this was attributed to subsidence of warm air from the free atmosphere. From aircraft measurements, Weigel and Rotach (2004) were able to confirm strong heating due to subsidence, but the limited temporal and spatial resolution in the observation data did not allow a thorough analysis of the processes leading to the observed thermal structure. This deficiency can now be overcome with ARPS, which has been shown to reproduce well both the general feature of a suppressed mixed layer growth and the complicated flow and circulation structure. The model output can thus be used to analyze the heat budget of the atmosphere over the valley floor and to evaluate the processes which lead to the stabilization of the temperature profiles.

b. Profiles of heat budget components over the valley floor

To investigate the physical reasons for the inhibited mixed layer growth, the terms of the potential temperature (θ) equation are extracted from the model and analyzed. Neglecting heating due to moist processes (on all three days the simulated valley atmosphere is basically cloud-free on the 350 m grid), this equation reads:

$$\frac{\partial \theta}{\partial t} = -u \frac{\partial \theta}{\partial x} - v \frac{\partial \theta}{\partial y} - w \frac{\partial \theta}{\partial z} - T - R . \quad (1)$$

The coordinate system is oriented such that the x-axis points cross-valley (normal to the valley axis) and the y-axis is along-valley (aligned with the valley axis). The hor-

horizontal wind components, u and v , are defined accordingly. The left hand side of this equation is the overall heating rate. The terms on the right hand side are heating (cooling) due to cross-valley advection of potential temperature, along-valley advection, vertical advection, subfilter-scale turbulent heat flux divergence (T) and radiation flux divergence (R). For greater readability, ‘subfilter-scale turbulence’ is henceforth simply referred to as ‘turbulence’. The overall heating rate, total advection, T and R are directly obtained from the model, and the individual advection components in the valley coordinate system are calculated from the output fields of velocity and potential temperature.

Fig. 10a shows the profiles of the heating (cooling) contribution terms of Eq. (1) on the late morning of 21 August. The profiles are averaged over 90 minutes (centered at 0945 UTC) over the valley floor width in slice ‘S150’ (shown in Fig. 1b; ‘S’ refers to the location of the slice in the southern valley half, and ‘150’ to data with horizontal grid spacing of 150 m). The individual contributions of the three advection components in the valley coordinate system are shown in Fig. 10b. Radiation flux divergence is not plotted, as its contribution to the total heat budget was found to be negligibly small. It can be seen that the valley atmosphere experiences a net warming over the whole valley depth and up to about 2500 m. The warming is almost entirely due to vertical advection, apart from the lowest 100 m where turbulent heat flux divergence is the dominant heating source. The net heating rate has its maximum ($5 \cdot 10^{-4} K s^{-1}$) close to the ground. On the mornings of the 22nd and the 25th of August, the profiles of the heat budget components reveal the same behavior (not shown). Analogous calculations have been carried out in a second slice in the northern half of the valley (‘N150’, see Fig. 1b), yielding equivalent results (not shown). This is not surprising, because the different circulation patterns illustrated in Fig. 8 are not yet established in the late morning, i.e. S150 and N150 are characterized by similar flow conditions.

Afternoon profiles (averaged over 90 minutes, centered at 1245 UTC) of the heat

budget components in slice S150 on the three simulation days are displayed in Fig. 11 together with the corresponding advection components. As in the morning profiles, the valley atmosphere experiences a relatively homogenous net heating rate through almost the entire valley depth. Its magnitude is on the order of $2 \cdot 10^{-4} K s^{-1}$, but in contrast to the morning situation, the heating rate is lower rather than higher close to the ground (on the order of $0.5 - 1.5 \cdot 10^{-4} K s^{-1}$ in the lowest 200 - 300 m above surface). Turbulent heat flux divergence dominates as a source of heating in this close-to-surface layer, which hereafter will be referred to as the TFDL (turbulent flux divergence layer). The strong turbulent heating in the TFDL is almost entirely balanced by advective cooling, resulting in a comparatively small net heating rate. The advective cooling in the TFDL is mainly due to vertical advection, partially also due to along-valley advection (Figs. 11d-f). Above the TFDL, the sign of the vertical advection changes, and it becomes the main contributor to the net heating rate, strong enough to offset the cooling effect of horizontal (mainly along-valley) advection. This is particularly evident in Fig. 11(e). Except for on 22 August, cross-valley advection is mostly negative and of smaller magnitude than the other advection components.

Through most of the valley atmosphere, the corresponding profiles of the heat budget components in slice N150 reveal characteristics similar to those in S150. This is shown here for the example of 22 August (Fig. 12). As in S150, heating due to turbulent flux divergence is restricted to a shallow TFDL at the surface, and vertical advection is the dominant heating source through the rest of the valley atmosphere, i.e. above the TFDL, balancing the strong advective cooling in the along-valley direction. In the TFDL, however, all three advection components have opposite sign between N150 and S150, and the net heating rate at N150 is about twice as large as at S150 ($2 \cdot 10^{-4} K s^{-1}$ instead of $1 \cdot 10^{-4} K s^{-1}$). The same behavior is observed on 21 and 25 August (not shown). The larger overall heating rate in the TFDL of slice N150 compared to S150 appears to be primarily due to the fact that in N150 vertical

advection does not become negative and thus does not contribute to the net advective cooling.

c. Discussion

One of the most notable features of the heat budget analysis is the almost uniform heating rate through the upper three quarters of the valley atmosphere. In the morning (Fig. 10) the air next to the surface experiences the highest heating rate, eventually leading to destabilization and thus to the growth of a well-mixed layer. In the afternoon, the net heating rate at the ground is significantly reduced compared to the morning. It is still positive, but its magnitude is comparable to, and in the southern valley half even lower than, the relatively uniform ‘background’ heating through the rest of the valley atmosphere (Fig. 11 and 12). In such a situation, further destabilization of the surface air which would further enhance convective mixing is not possible. Our observation of a suppressed mixed-layer growth in the afternoons (Section 4a) is thus reflected in the profiles of net heating rate. To understand this behavior, two aspects need to be considered: (a) the positive uniform heating rate over almost the entire valley depth, and (b) the reduced heating rate on the surface despite positive surface heat fluxes.

The first aspect is clearly attributed to the subsidence of potentially warmer air (i.e., air with a higher potential temperature). Consistent with the idealized simulations of Rampanelli et al. (2004), this can be explained by the existence of slope winds. Air is carried out of the valley along the slopes and replaced by subsiding air in the valley center. The slope winds actually overshoot into the free atmosphere. This is shown for 21 August in Fig. 13, which shows contours of vertical velocity in a slice across the ridge east of surface station A1. Boundary layer air is vented into the free atmosphere in the manner described for example by Kossmann et al. (1999) or

Henne et al. (2004). This explains why the subsidence heating dominates well above the crest height. Mountain venting begins in the morning hours, which is consistent with observations of De Wekker et al. (2004) in the Jungfraujoeh region in central Switzerland.

The other aspect leading to the observed stabilization of the valley atmosphere is the reduced net surface heating, which becomes effective in the afternoon once the strong up-valley winds have started. Being thermally driven, these winds advect potentially colder air up the valley axis. Above the TFDL, subsidence is strong enough to balance the cooling effect of the valley winds, resulting in a net positive advective heating contribution. Within the TFDL, the process appears to be more complicated, and a distinction needs to be made between the effects of the different flow and circulation patterns described in Section 3.

In slice N150, the up-valley wind is uniformly spread over the valley floor. The wind speed and thus the cooling next to the ground are relatively large (on the order of $5 \cdot 10^{-4} K s^{-1}$ on all three simulation days). Moreover, the thermally-driven cross-valley circulation carries near-surface air from the shaded east-facing slope to the sunlit west-facing side, thus providing additional cooling. Close to the surface, subsidence heating is not strong enough to balance these cooling contributions. In slice S150, the situation is different: as has been explained in Section 3a, the core of the valley wind is pushed from the valley center to the right over the sunlit heated west-facing slope. Thus, in the valley center, the cooling due to along-valley advection is reduced compared to N150. It can even be of opposite sign (Fig. 11e), because north of S150 the cold up-valley jet tends to meander back towards the valley center, leading to locally negative gradients in potential temperature in the along-valley direction. The curvature-induced clockwise secondary circulation, if strong enough, can lead to cross-valley advective heating, as the near-surface cross-valley flow comes from the west-facing sunlit slope (Fig. 11d,e). Moreover, this circulation advects potentially

colder air from the ‘lifted’ core of the up-valley jet down to the ground (Fig. 6d and 7), resulting in the strong negative vertical advection which is observed on all three days in the TFDL (Figs. 11d-f).

The lower surface heating rates in slice S150 compared to N150 show that the secondary circulation is a strong mechanism for surface-cooling, stronger than the ‘undisturbed’ along-valley advection of potentially colder air in slice N150. Consequently, the depth of the atmospheric boundary layer in the Riviera Valley is highly dependent on the exact position in the valley and the local circulation structure. Figure 14 shows the variation of well-mixed layer thickness in the along-valley direction, as obtained on 22 August at 1245 UTC on the 350 m grid. The position-dependent differences between the southern and the northern part of the valley are apparent. In the northern part of the valley, the well-mixed layer (shaded area) is only about 200 m thick; however, in the southern part, under the influence of the curvature-induced secondary circulation, it is even shallower (50-100 m). The same qualitative picture holds on 21 and 25 August. Due to its high spatial variability, the thickness of the well-mixed layer, as measurable from radiosondes (i.e. at a given location), is thus not a representative length scale for the atmospheric boundary layer in the entire valley.

5. Total heat budget

a. *Time evolution of the valley heat budget*

Finally, we examine the processes which contribute to the heating of the Riviera Valley atmosphere as a whole, and thus ultimately determine the onset and strength of valley winds (if we assume them to be purely thermally driven). We therefore extend our analysis to a larger volume on the 350 m simulation grid which contains the major part of the Riviera Valley. We have chosen volume V350, as outlined in Fig. 1a, for

the integration volume. The east and west boundaries of the volume are chosen such that they approximately follow the two ridge-lines which frame the valley. On the 350 m grid, the altitude of these two ridges varies between approximately 2000 m and 2500 m. The depth of volume V350 extends from the valley floor up to an altitude of 2000 m. The north and south boundaries of V350 are set locally perpendicular to the valley axis.

The volume-averaged and density-weighted heat budget components are calculated according to following equation, which is based on Eq. (1):

$$\underbrace{\frac{1}{M_V} \cdot \iiint_{V350} \rho \cdot \frac{\partial \theta}{\partial t} dV}_{\text{net heating rate}} = \underbrace{-\frac{1}{M_V} \cdot \iiint_{V350} \rho \left(u \frac{\partial \theta}{\partial x} + v \frac{\partial \theta}{\partial y} + w \frac{\partial \theta}{\partial z} \right) dV}_{\text{total advection}} - \underbrace{\frac{1}{M_V} \cdot \iiint_{V350} \rho \cdot T dV}_{\text{turb. heat flux div.}} - \underbrace{\frac{1}{M_V} \cdot \iiint_{V350} \rho \cdot R dV}_{\text{radiation flux div.}} . \quad (2)$$

M_V is the total mass of air in V350, and ρ is the density. The time-series of the heat budget components in volume V350 on 21 August are shown in Fig. 15. Similar to earlier plots, the individual advection components in the valley coordinate system are displayed separately. In Fig. 15a, it can be seen that the dominant source of heating is turbulent heat flux divergence. This result is plausible, because turbulent flux divergence has to balance the total surface heat flux, but it appears to be contradictory to the findings of Section 4c, where the shallowness of the TFDL and the large vertical advective heating over the valley base were emphasized. The paradox can be understood by recalling that the valley side-walls are not contained in slices S150 and N150, but are included here in V350. Over the slopes, turbulent heat flux divergence is consistently strong and positive (not shown), while the heat budget contribution of vertical advection is mainly negative (due to up-slope winds). This means that, av-

eraged over V350, turbulent heat flux divergence gains in importance with respect to vertical advective heating.

The daytime evolution of turbulent heat flux divergence smoothly follows the pattern of incoming solar radiation. The maximum ($1.5 \cdot 10^{-4} K s^{-1}$) occurs at around 1230 UTC. Radiation flux divergence, on the other hand, is almost negligible. Total advection, finally, is only the dominant source of heating until about 0900 UTC. After that, it quickly decreases and changes sign at about 1100 UTC. Its maximum is only half the magnitude of the maximum turbulent flux divergence. The advection components in the valley coordinate system (Fig. 15b) show that vertical and along-valley advection are of considerable magnitude, while cross-valley advection is relatively small. Vertical advection is a constant source of heating until about 1600 UTC, while along-valley advection continuously cools the valley. Net cooling begins at approximately 1600 UTC.

The results obtained for 22 August (Fig. 16) and 25 August (Fig. 17) generally follow 21 August apart from a few details. On 22 August, the magnitude of turbulent flux divergence is larger than on 21 August (achieving a maximum value of $2 \cdot 10^{-4} K s^{-1}$), while total advection is comparatively weak. It dominates over turbulent flux divergence only until about 0800 UTC and does not exceed a maximum heating rate of $0.5 \cdot 10^{-4} K s^{-1}$. On 25 August, on the other hand, advection is very strong and dominant (on the order of $1.5 \cdot 10^{-4} K s^{-1}$) until about 0900 UTC before it drops sharply and changes sign.

An analysis of the along-valley variability of the heat budget components (not shown) reveals that the observed characteristics are relatively independent of the circulation regime in the lower valley atmosphere. This means that the overall valley heat budget is not significantly affected by the sense of rotation of the underlying cross-valley circulation, i.e. on whether the circulation is thermally driven or curvature-induced.

b. Discussion

The volume argument of the TAF concept implies that no heat is exchanged with the free atmosphere above the valley, meaning that the valley atmosphere heats entirely due to turbulent heat flux divergence, because advection would only redistribute heat within a closed circulation. If we assume negligible variation of density with time (justified in the frame of the shallow motion approximations, Mahrt 1986), and if we assume the volume argument to hold, then the sum of vertical and cross-valley advection must be zero. The heat budget analysis has shown that turbulent flux divergence (averaged over V350) is indeed an important contributor to the overall heating rate. Vertical advection, however, is also consistently positive (until about 16-17 UTC) and has a magnitude which is on the order of or even larger than the effect of turbulent heat flux divergence. Cross-valley advection is negative, but has only a comparatively small magnitude, meaning that the sum of vertical and cross-valley advection is positive and clearly non-zero. This can only be explained by subsidence of potentially warmer air from the free atmosphere through the valley top (as proposed in Section 4c), which violates the volume argument of the TAF concept. Given the strong cooling due to along-valley advection, the net heating rate and thus the valley temperature would be lower without the effect of subsidence heating. This would lead to a reduced valley-plain temperature gradient and thus weaker up-valley winds.

In the case of significant net vertical export of valley air through the upper boundary of V350, the vertical advection term in the heat budget becomes negative. This is for example the case on 21 August after 17 UTC, when a mass budget analysis (not shown) reveals strong vertical mass fluxes on the order of $0.07 \text{ kg s}^{-1} \text{ m}^{-2}$. North of the Riviera Valley, i.e. closer towards the central Alps, the valleys become smaller and are characterized by significantly sloped floors and decreasing widths. Consistent with classical valley flow theory, strong rising motions can be expected in such narrow-

ing valleys during up-valley flow periods, connecting the flow layer within the valleys with a larger-scale return flow layer above. This means that once valley winds have started, the heat budgets in those valleys may well be different from our Riviera Valley observations.

We now evaluate the structure of the heat budget in the hours before the onset of up-valley winds in the morning, i.e. before 0900-1000 UTC. On 21 and 25 August, advective heating (solely due to subsidence) rather than turbulent flux divergence is the dominant contributor to the net heating rate during this time. Therefore, on these two days the warming of the Riviera atmosphere appears to support the concept of Rampanelli et al. (2004), according to which subsidence leads to the heating necessary for the development of thermally driven up-valley winds. On the morning of 22 August, the situation is less clear, as subsidence is relatively low and turbulent flux divergence dominates over net advective heating from about 0730 UTC. This means that on this day the up-valley winds are probably initiated due to a combination of subsidence heating and turbulence heating.

The strength of subsidence heating itself is determined by two factors: the subsidence velocity and the stratification of the valley atmosphere. On 21 and 22 August, the average gradients of potential temperature in the valley atmosphere at 0800 UTC are of comparable magnitude (around 0.004 K m^{-1}), but the subsidence velocity is higher on 21 August (0.05 m s^{-1}) than on 22 August (0.03 m s^{-1}), explaining the stronger subsidence heating on 21 August. Comparable subsidence velocities are found on 22 and 25 August, but 25 August is much more stably stratified (0.0066 K m^{-1}). Due to the larger vertical gradient of potential temperature, 25 August experiences more subsidence heating than 22 August. To quantify the effect of subsidence heating in the general case, it would be necessary to analyze the factors determining the strength of the slope flows and thus of subsidence velocity. This has not been done here, but aspects such as Bowen ratio, stability (Whiteman et al. 2004) and the mixing

of momentum from the top of the valley (Egger 1990) are expected to be of importance in this context.

6. Summary and conclusions

The LES-code ‘ARPS’ has been applied to simulate and investigate the daytime atmosphere in the Riviera Valley on three summer days with fair weather conditions and pronounced thermally driven up-valley winds. The performance of the code has been evaluated with comparisons to data from the MAP-Riviera field campaign. From our work, we can conclude that ARPS is able to reproduce both the thermal and dynamic features of the atmosphere over topography as steep and complex as the Riviera Valley. This not only refers to the stratification and surface winds (shown in Part I by Chow et al. 2005), as the model also captures very distinct circulation patterns. These patterns have been identified from airborne measurements and include thermally driven cross-valley circulations as well as a curvature-induced secondary circulation at the southern valley mouth (summarized in Fig. 8). Given the good performance of ARPS, the components contributing to the heat budgets have been investigated. The major findings can be summarized as follows:

(i) The growth of a well-mixed layer in the Riviera Valley is suppressed (Fig. 9). Despite positive surface heat fluxes, the valley atmosphere has a tendency to stabilize. Turbulent heat flux divergence as a source of heating is restricted to a shallow layer of only 100-300 m depth above the ground and the slopes. These observations are due to the combined effect of cold-air advection in the up-valley direction and subsidence of warm air from the free atmosphere aloft (Fig. 12b). The subsidence is a consequence of thermally driven slope winds.

(ii) The existence of a curvature-induced secondary circulation in the southern half of the valley further stabilizes the near-surface valley atmosphere compared to

the northern valley half. Consequently, the well-mixed layer can vary considerably in depth along the valley, depending on the geographic position and the overlying circulation pattern (Fig. 14). Therefore, the mixed-layer depth, as obtained from point measurements (e.g. from radiosondes), is not a representative length scale for the atmospheric boundary layer of the entire valley.

(iii) Subsidence of warm air from the free atmosphere above the valley is one of the main heating sources in the heat budget of the entire valley atmosphere (Figs. 15, 16, 17). Subsidence heating typically reaches about $2 \cdot 10^{-4} \text{ K s}^{-1}$ in mid-afternoon and is of comparable or even larger magnitude than turbulent heat flux divergence. It compensates for most of the cooling due to along-valley advection. Therefore, a positive net heating rate can be maintained throughout the afternoon. This is a prerequisite for the persistence of valley-plain temperature gradients and thus of strong thermally driven up-valley winds until the evening.

(iv) On the mornings of two out of the three observation days, subsidence has been identified as the *only* major heating source of the valley atmosphere prior to the onset of valley-winds (Figs. 15 and 17). Thus, the build-up of a valley-plain temperature gradient cannot be explained by the ‘topographic amplification factor’ concept alone, at least not in the Riviera Valley. Our observations support the subsidence concept of Rampanelli et al. (2004) as an essential mechanism of valley warming.

These conclusions are solely drawn from an analysis of the processes in the Riviera Valley, which is part of a large and widely branched valley system. As the Riviera Valley is located in the center of this valley system and is of medium size, the processes observed in the Riviera Valley are likely to be similar to those found in other valleys of the system, as long as the flow conditions are comparable. Nevertheless, it would be desirable to carry out a comparable heat budget analysis on the entire valley system. Moreover, in order to quantify and generalize the relevance of subsidence heating, a thorough analysis of the factors determining the strength of cross-valley circulations

under real conditions is necessary. LES has been shown to be a useful tool in this context.

ACKNOWLEDGMENTS

This work has been supported by the Swiss National Science Foundation (grants #20-68320.01 and #20-100013) [APW], by a National Defense Science and Engineering Graduate fellowship [FKC] and NSF Grants ATM-0073395 [FKC and RLS] and ATM-0129892 [MX]. We gratefully acknowledge the National Center for Atmospheric Research (sponsored by the NSF) for providing the computing time used in this research. Finally, we thank Massimiliano Zappa and Karsten Jasper for their great help in applying WASIM-ETH on the Riviera topography.

References

- Barry, R. G.: 1992, *Mountain weather and climate*, Routledge, London and New York. 2nd edition.
- Chow, F. K., A. P. Weigel, R. L. Street, M. W. Rotach, and M. Xue, 2005: High-resolution large-eddy simulations of flow in a steep alpine valley. Part I: Methodology, verification and sensitivity studies. *J. Appl. Meteor.*, **submitted for publication**.
- De Wekker, S. F. J., D. G. Steyn, J. D. Fast, M. W. Rotach, and S. Zhong, 2005: The performance of RAMS in representing the convective boundary layer structure in a very steep valley. *Environ. Fluid Mech.*, **5**, 35–62.
- De Wekker, S. F. J., D. G. Steyn, and S. Nyeki, 2004: A comparison of aerosol-layer

- and convective boundary-layer structure over a mountain range during STAAARTE '97. *Bound.-Layer Meteor.*, **113**, 249–271.
- Egger, J.: 1990, Thermally forced flows: Theory. *Atmospheric processes over complex terrain*, W. Blumen, ed., American Met. Soc., Boston, 43–58.
- Fast, J. D., S. Zhong, and C. D. Whiteman, 1996: Boundary layer evolution within a canyonland basin. Part II: Numerical simulations of nocturnal flows and heat budgets. *J. Appl. Meteor.*, **35**, 2162–2178.
- Geyer, W. R., 1993: Three-dimensional tidal flow around headlands. *J. Geophys. Res.*, **98 (C1)**, 955–966.
- Gohm, A., G. Zängl, and G. J. Mayr, 2004: South Foehn in the Wipp Valley on 24 October 1999 (MAP IOP 10): Verification of high-resolution numerical simulations with observations. *Mon. Wea. Rev.*, **132**, 78–102.
- Henne, S., M. Furger, S. Nyeki, M. Steinbacher, B. Neininger, S. F. J. de Wekker, J. Dommen, N. Spichtinger, A. Stohl, and A. S. H. Prévôt, 2004: Quantification of topographic venting of boundary layer air to the free troposphere. *Atmos. Chem. Phys.*, **4**, 497–509.
- Hennemuth, B., 1987: Heating of a small Alpine valley. *Meteor. Atmos. Phys.*, **36**, 287–296.
- Jasper, K., 2001: *Hydrological modelling of alpine river catchments using output variables from atmospheric models*. Published dissertation no. 14385, Swiss Federal Institute of Technology (ETH), Zurich, Switzerland.
- Kalkwijk, J. P. T. and R. Booij, 1986: Adaptation of secondary flow in nearly-horizontal flow. *J. Hydraul. Res.*, **24**, 19–37.

- Kalthoff, N., V. Horlacher, U. Corsmeier, A. Volz-Thomas, B. Kolahgar, H. Geiß, M. Möllmann-Coers, and A. Knaps, 2000: Influence of valley winds on transport and dispersion of airborne pollutants in the Freiburg-Schauinsland area. *J. Geophys. Res.*, **105 (D1)**, 1585–1597.
- Kossmann, M., U. Corsmeier, S. F. J. de Wekker, F. Fiedler, N. Kalthoff, H. Güsten, and B. Neininger, 1999: Observation of handover processes between the atmospheric boundary layer and the free troposphere over mountainous terrain. *Contrib. Atmos. Phys.*, **72**, 329–350.
- Kuwagata, T. and F. Kimura, 1995: Daytime boundary layer evolution in a deep valley. Part I: Observations in the Ina Valley. *J. Appl. Meteor.*, **34**, 1082–1091.
- 1997: Daytime boundary layer evolution in a deep valley. Part II: Numerical simulation of the cross-valley circulation. *J. Appl. Meteor.*, **36**, 883–895.
- Mahrt, L., 1986: On the shallow motion approximations. *J. Atmos. Sci.*, **43**, 1036–1044.
- Matzinger, N., M. Andretta, E. Van Gorsel, R. Vogt, A. Ohmura, and M. W. Rotach, 2003: Surface radiation budget in an Alpine valley. *Quart. J. Roy. Meteor. Soc.*, **129**, 877–895.
- McKee, T. B. and R. D. O’Neil, 1989: The role of valley geometry and energy budget in the formation of nocturnal valley winds. *J. Appl. Meteor.*, **28**, 445–456.
- Neininger, B., 1982: Mesoklimatische Messungen im Oberwallis. *Int. Tagung für Alpine Meteorologie, Berchtesgaden, DWD, Ann. Meteor.*, **19**, 105–107.
- Neininger, B., W. Fuchs, M. Bäumle, A. Volz-Thomas, A. S. H. Prévôt, and J. Domen: 2001, Paper 5.7: A small aircraft for more than just ozone: MetAir’s ‘Dimona’

- after ten years of evolving development. *Proceedings of the 11th Symposium on Meteorological Observations and Instrumentation, Amer. Met. Soc.*, Albuquerque, NM, 123–128.
- Pielke, R. A., W. R. Cotton, R. L. Walko, C. J. Tremback, W. A. Lyons, L. D. Grasso, M. E. Nicholls, M. D. Moran, D. A. Wesley, T. J. Lee, and J. H. Copeland, 1992: A comprehensive meteorological modeling system – RAMS. *Meteor. Atmos. Phys.*, **49**, 69–91.
- Rampanelli, G., D. Zardi, and R. Rotunno, 2004: Mechanisms of up-valley winds. *J. Atmos. Sci.*, **61**, 3097–3111.
- Rotach, M. W., P. Calanca, G. Graziani, J. Gurtz, D. G. Steyn, R. Vogt, M. Andretta, A. Christen, S. Cieslik, R. Connolly, S. F. J. De Wekker, S. Galmarini, E. N. Kadygrov, V. Kadygrov, E. Miller, B. Neininger, M. Rucker, E. van Gorsel, H. Weber, A. Weiss, and M. Zappa, 2004: The turbulence structure and exchange processes in an Alpine valley: The Riviera project. *Bull. Amer. Met. Soc.*, **85**, 1367–1385.
- Rozovskii, I. L., 1957: Dvizhenie vody na povorote otkrytogo rusla. *Izd. Akad. Nauk. Ukr. SSR, Kiev* (English translation 1961: Flow of water in bends of open channels. *Israel Progr. Sci. Transl., Jerusalem*).
- Steinacker, R., 1984: Area-height distribution of a valley and its relation to the valley wind. *Contrib. Atmos. Phys.*, **57**, 64–71.
- Vergeiner, I. and E. Dreiseitl, 1987: Valley winds and slope winds - observations and elementary thoughts. *Meteor. Atmos. Phys.*, **36**, 264–286.
- Wagner, A., 1938: Theorie und Beobachtung der periodischen Gebirgswinde. *Gerlands Beitr. Geophys.*, **52**, 408–449.

- Weigel, A. P. and M. W. Rotach, 2004: Flow structure and turbulence characteristics of the daytime atmosphere in a steep and narrow Alpine valley. *Quart. J. Roy. Meteor. Soc.*, **130**, 2605–2627.
- Whiteman, C. D.: 1990, Observations of thermally developed wind systems in mountainous terrain. *Atmospheric processes over complex terrain*, W. Blumen, ed., American Met. Soc., Boston, 5–42.
- 2000, *Mountain Meteorology. Fundamentals and applications*, Oxford University Press, New York, Oxford.
- Whiteman, C. D., T. B. McKee, and J. C. Doran, 1996: Boundary layer evolution within a canyonland basin. Part I: Mass, heat and moisture budgets from observations. *J. Appl. Meteor.*, **35**, 2145–2161.
- Whiteman, C. D., B. Pospichal, S. Eisenbach, P. Weihs, C. B. Clements, R. Steinacker, E. Mursch-Radlgruber, and M. Dorninger, 2004: Inversion breakup in small Rocky Mountain and Alpine basins. *J. Appl. Meteor.*, **43**, 1069–1082.
- Whiteman, C. D., S. Zhong, X. Bian, J. D. Fast, and J. C. Doran, 2000: Boundary layer evolution and regional-scale diurnal circulations over the Mexico Basin and Mexican plateau. *J. Geophys. Res.*, **105 (D8)**, 10081–10102.
- Xue, M., K. K. Droegemeier, and V. Wong, 2000: The Advanced Regional Prediction System (ARPS) - A multi-scale nonhydrostatic atmospheric simulation and prediction model. Part I: Model dynamics and verification. *Meteor. Atmos. Phys.*, **75**, 161–193.
- Xue, M., K. K. Droegemeier, V. Wong, A. Shapiro, K. Brewster, F. Carr, D. Weber, Y. Liu, and D. Wang, 2001: The Advanced Regional Prediction System (ARPS)

- A multi-scale nonhydrostatic atmospheric simulation and prediction tool. Part II: Model physics and applications. *Meteor. Atmos. Phys.*, **76**, 143–165.

Xue, M., D. H. Wang, J. D. Gao, K. Brewster, and K. K. Droegemeier, 2003: The Advanced Regional Prediction System (ARPS), storm-scale numerical weather prediction and data assimilation. *Meteor. Atmos. Phys.*, **82**, 139–170.

Zängl, G., B. Chimani, and C. Häberli, 2004: Numerical simulations of the foehn in the Rhine Valley on 24 October 1999 (MAP IOP 10). *Mon. Wea. Rev.*, **132**, 368–389.

List of Tables

- 1 Root-mean-square-errors (rmse) and mean errors (bias) for simulations compared to measurements at surface station A1. θ is the potential temperature, U the wind speed and Φ the wind direction. 46 half-hourly values (beginning at 0015 UTC) have been used to calculate bias and rmse. The high values in Φ rmse are primarily due to light night-time winds, leading to large directional fluctuations. 30
- 2 Root-mean-square-errors (rmse) and mean errors (bias) for potential temperature θ for radio soundings up to 6 km from surface station A1. 31

	θ rmse	θ bias	U rmse	U bias	Φ rmse	Φ bias
	(K)	(K)	(ms^{-1})	(ms^{-1})	($^{\circ}$)	($^{\circ}$)
21 August	2.18	-1.76	2.41	-1.67	54.82	3.01
22 August	0.88	-0.19	1.80	-1.03	90.44	-7.93

Table 1: Root-mean-square-errors (rmse) and mean errors (bias) for simulations compared to measurements at surface station A1. θ is the potential temperature, U the wind speed and Φ the wind direction. 46 half-hourly values (beginning at 0015 UTC) have been used to calculate bias and rmse. The high values in Φ rmse are primarily due to light night-time winds, leading to large directional fluctuations.

Sounding time (UTC)	0000	0600	0900	1200	1500	1800	2100	All
21 Aug: θ rmse (K)	2.12	1.47	0.78	0.91	0.76	1.19	1.36	1.23
21 Aug: θ bias (K)	0.73	0.73	0.17	-0.14	-0.49	0.50	0.42	0.28
22 Aug: θ rmse (K)	1.44	1.05	0.61	0.73	0.65	0.53	0.97	0.85
22 Aug: θ bias (K)	0.66	0.62	-0.06	0.04	0.02	0.41	0.65	0.32

Table 2: Root-mean-square-errors (rmse) and mean errors (bias) for potential temperature θ for radio soundings up to 6 km from surface station A1.

List of Figures

- 1 Topography of (a) the 350 m grid and (b) the 150 m grid. ‘A1’ denotes the location of a surface measurement station (Bosco di Sotto). Data extracted from slices ‘S150’ and ‘N150’ are used in Section 4b. ‘V350’ indicates the integration volume used in Section 5. 36
- 2 Measured (black) and simulated (grey) time-series of potential temperature (upper panels) and surface winds (lower panels) at observation site A1 on 21 August (left hand side) and 22 August (right hand side). The comparisons for 25 August are shown in Figs. 4 and 5 of Chow et al. (2005). 37
- 3 Observed radiosonde (solid line, ‘RS’) and simulated (dashed line, ‘ARPS’) profiles of potential temperature on 21 (upper panels) and 22 August (lower panels) at 0900 UTC, 1200 UTC and 1500 UTC. The grey bar indicates the crest height next to site A1. The corresponding profiles of 25 August are shown in Fig. 8 of Chow et al. (2005). 38
- 4 Up-valley wind vectors at an altitude of 900 m on 21 August (a) as measured by the aircraft and (b) as simulated with ARPS. The airborne data are interpolated from three along-valley legs flown between 1500 UTC and 1620 UTC. The simulated flow structure is from the model output at 1530 UTC. The background elevation contours in (b) show the smoothed topography on the 350 m model grid and therefore look slightly different from those in (a). In both plots, the elevation contours are in 200 m intervals. 39

5	Measured and simulated up-valley wind component in a valley cross-section about 3.5 km north of the southern valley entrance on 21, 22 and 25 August. The panels on the left hand side show airborne data and the panels on the right the corresponding simulation results. The measurement data have been obtained and interpolated from cross-valley flight legs in 8-11 levels of elevation. The grey line is the contour of zero along-valley velocity. Note the different grey scale on 25 August.	40
6	Simulated cross-valley wind vectors on 22 August in two slices across the Riviera Valley (as indicated on the small topography panels): one in the northern half of the valley (a,c), and one close to the southern valley mouth (b,d). The upper panels show the cross-valley flow at 0830 UTC, the lower ones at 1230 UTC. The shading indicates vertical wind velocity. The black line is the contour of zero vertical velocity.	41
7	Simulated cross-valley wind vectors in a slice close to the southern valley mouth on 21 August (a) and 25 August (b) at 1230 UTC. The shades of grey indicate vertical wind velocity. The black line is the contour of zero vertical velocity.	42
8	Schematic representation of the afternoon cross-valley flow in two cross-sections in the Riviera Valley (as indicated in the small topography-panels). (a) shows the thermally driven counter-clockwise circulation observed in the northern half of the valley, while (b) displays the curvature-induced clockwise secondary circulation of the southern valley entrance region.	43

9	Time-height plots of simulated vertical gradients of potential temperature on 25 August (contours labeled in $K m^{-1}$). The shading indicates neutral to super-adiabatic stratification. (a) is in the Riviera Valley (at site A1) and (b) at a location approximately 50 km southwest of the Riviera Valley (45.93°N, 8.77°E), i.e. at the beginning of the foothills of the Alps (obtained from the 1 km grid).	44
10	Simulated profiles of (a) the heat budget contributions and (b) the respective advection terms in the valley coordinate system on the late morning of 21 August. The profiles are 90-minutes averages (centered at 0945 UTC) over the valley base width in slice S150 (see Fig. 1b). The grey bar indicates the crest height.	45
11	Simulated profiles of the heat budget contributions (upper row) and the respective advection terms in the valley coordinate system (lower row) on the afternoons of 21 August (a,d), 22 August (b,e) and 25 August (c,f). The profiles are 90-minutes averages (centered at 1245) over the valley base width in slice S150 (see Fig. 1b). The grey bar indicates the crest height.	46
12	Simulated profiles of the heat budget contributions (a) and the respective advection terms in the valley coordinate system (b) on the afternoon of 22 August. The profiles are 90-minutes averages (centered at 1245 UTC) over the valley base width in slice N150 (see Fig. 1b). The grey bar indicates the crest height.	47
13	Simulated flow structure in a vertical slice across the ridge east of surface station A1, showing the venting of boundary layer air into the free atmosphere on 21 August at (a) 0945 UTC and (b) 1245 UTC. The contours indicate vertical wind velocity, with the black line being zero vertical velocity.	48

14	Variation of well-mixed layer thickness in the along-valley direction on 22 August at 1245 UTC as simulated with ARPS. The contours (labeled in $K m^{-1}$) show the vertical gradient of potential temperature, with areas of neutral or super-adiabatic stratification being shaded in grey. The position of the secondary circulation is indicated. Along-valley distance has an arbitrary origin at the town of Bellinzona (Fig. 1).	49
15	Time-series from simulations of (a) the heat budget components and (b) the advection components on 21 August, averaged over V350 on the 350 m grid (see Fig. 1b).	50
16	As Fig. 15, but for 22 August.	51
17	As Fig. 15, but for 25 August.	52

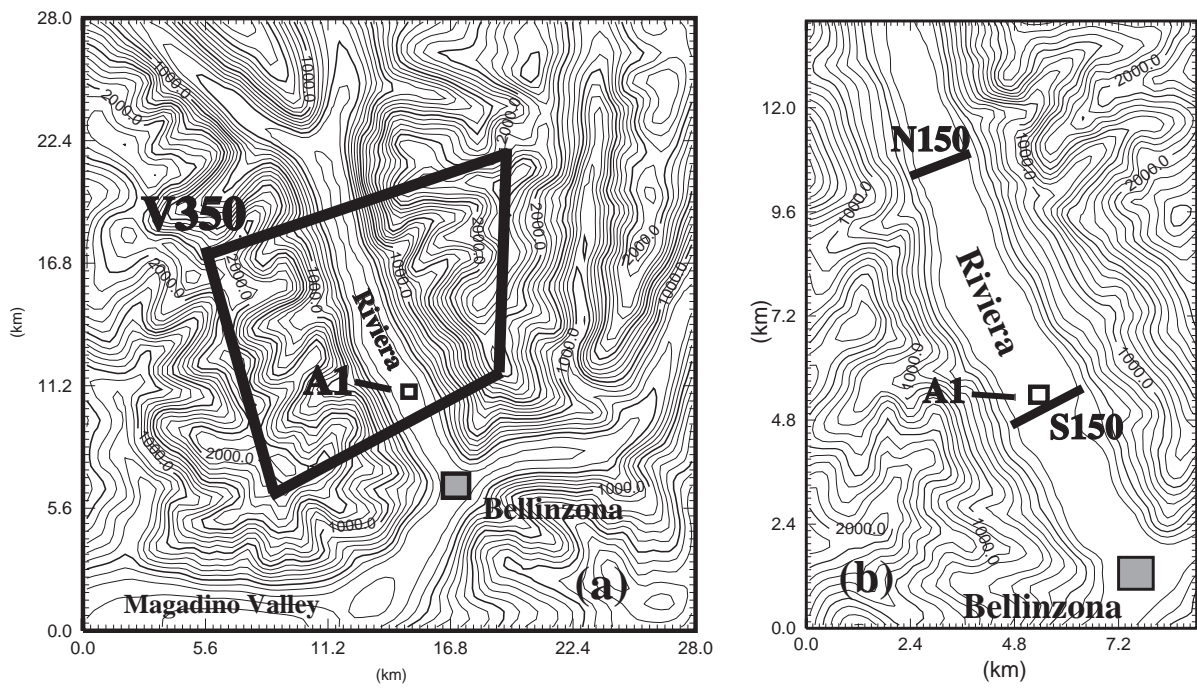


Figure 1: Topography of (a) the 350 m grid and (b) the 150 m grid. ‘A1’ denotes the location of a surface measurement station (Bosco di Sotto). Data extracted from slices ‘S150’ and ‘N150’ are used in Section 4b. ‘V350’ indicates the integration volume used in Section 5.

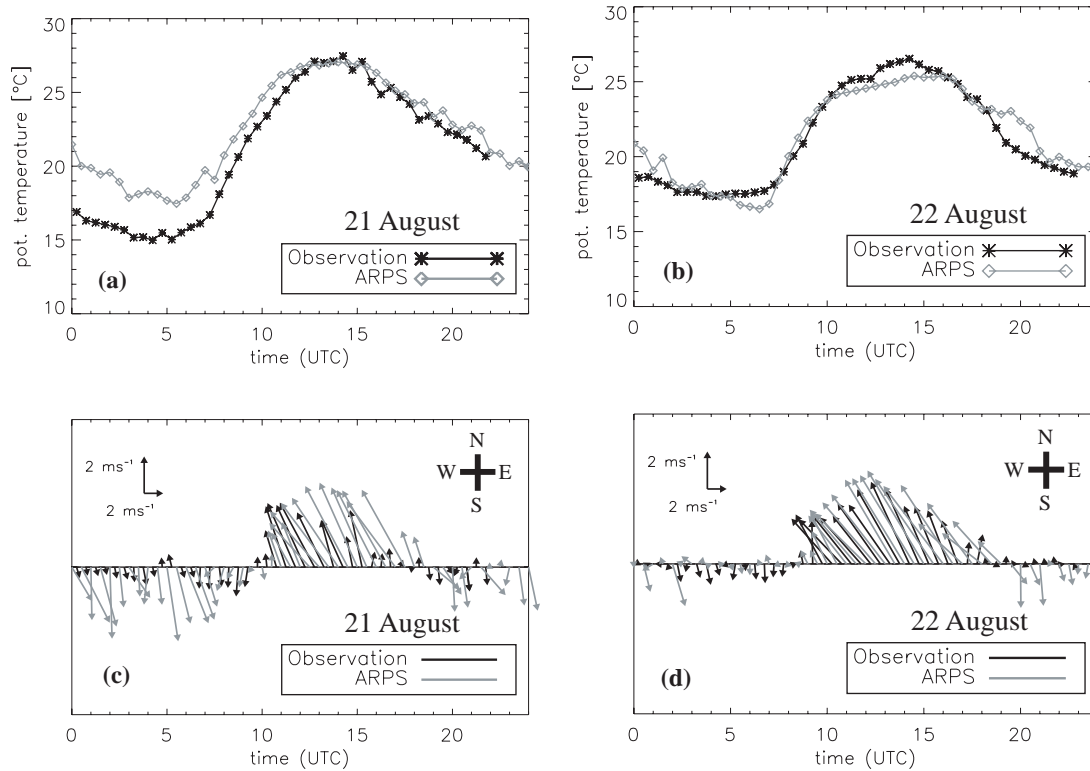


Figure 2: Measured (black) and simulated (grey) time-series of potential temperature (upper panels) and surface winds (lower panels) at observation site A1 on 21 August (left hand side) and 22 August (right hand side). The comparisons for 25 August are shown in Figs. 4 and 5 of Chow et al. (2005).

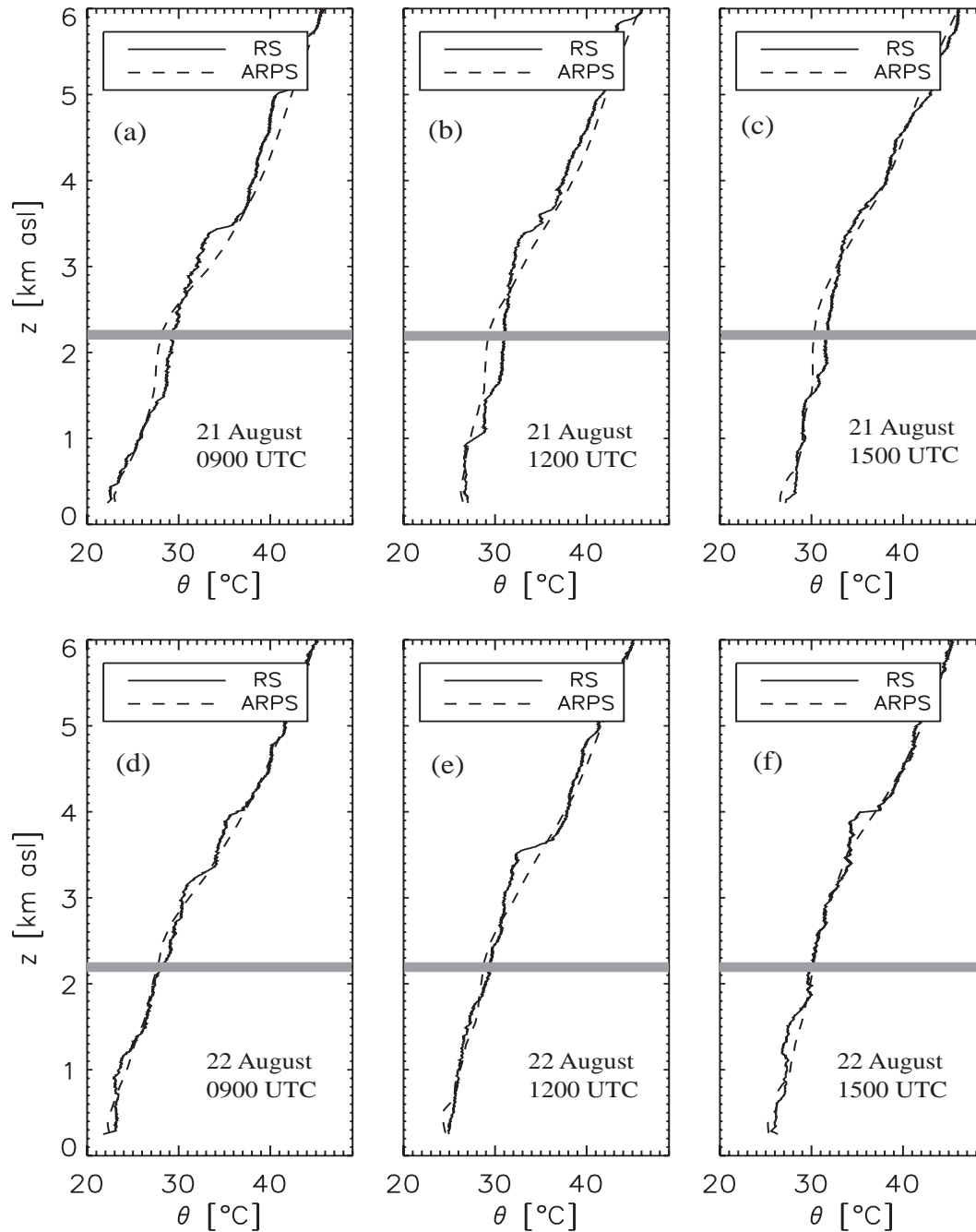


Figure 3: Observed radiosonde (solid line, ‘RS’) and simulated (dashed line, ‘ARPS’) profiles of potential temperature on 21 (upper panels) and 22 August (lower panels) at 0900 UTC, 1200 UTC and 1500 UTC. The grey bar indicates the crest height next to site A1. The corresponding profiles of 25 August are shown in Fig. 8 of Chow et al. (2005).

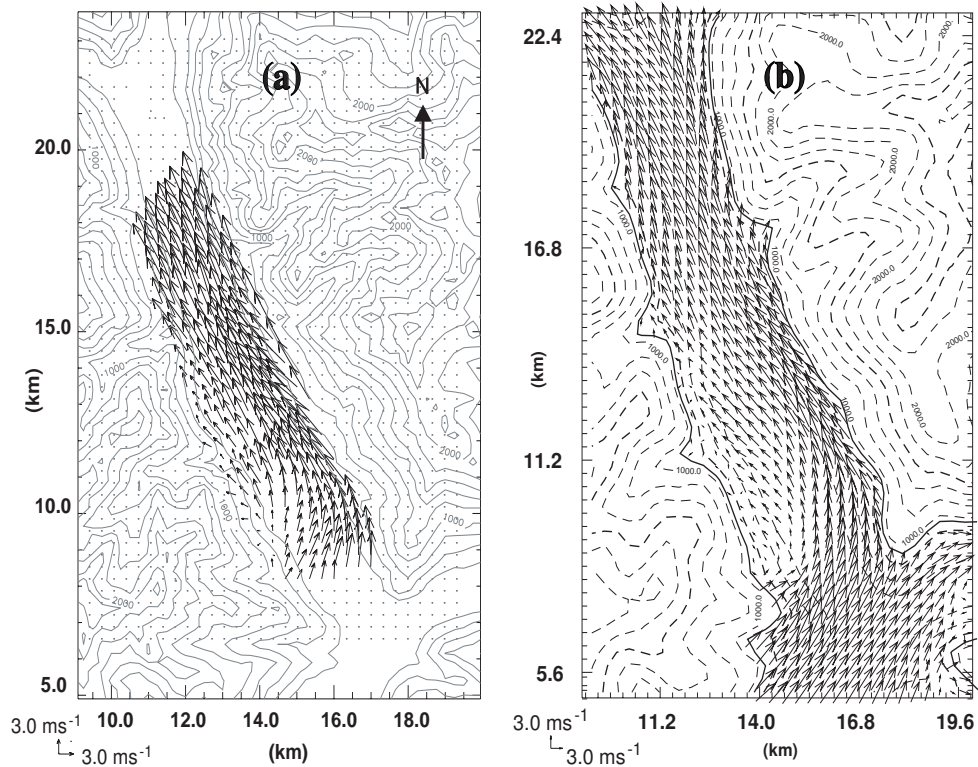


Figure 4: Up-valley wind vectors at an altitude of 900 m on 21 August (a) as measured by the aircraft and (b) as simulated with ARPS. The airborne data are interpolated from three along-valley legs flown between 1500 UTC and 1620 UTC. The simulated flow structure is from the model output at 1530 UTC. The background elevation contours in (b) show the smoothed topography on the 350 m model grid and therefore look slightly different from those in (a). In both plots, the elevation contours are in 200 m intervals.

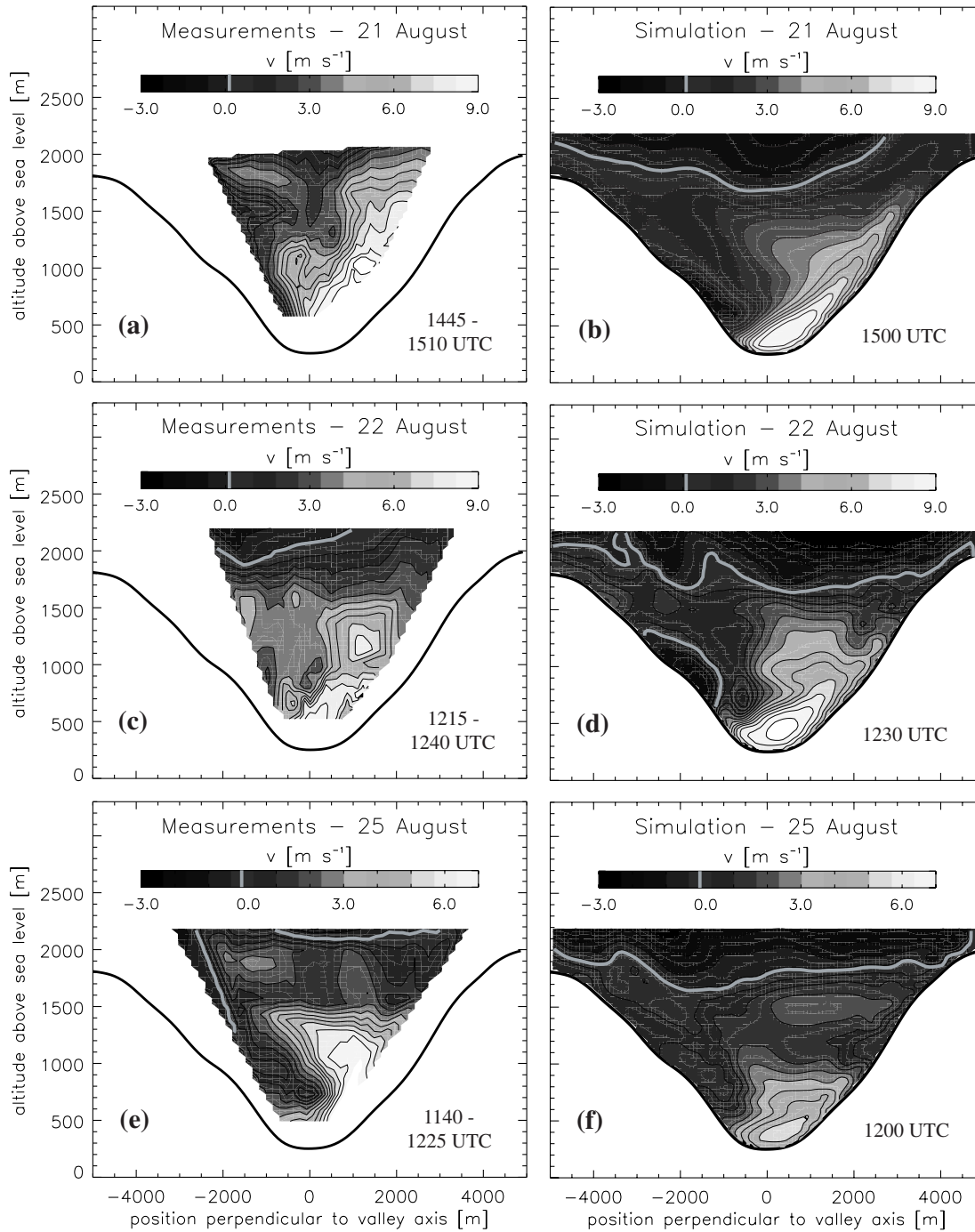


Figure 5: Measured and simulated up-valley wind component in a valley cross-section about 3.5 km north of the southern valley entrance on 21, 22 and 25 August. The panels on the left hand side show airborne data and the panels on the right the corresponding simulation results. The measurement data have been obtained and interpolated from cross-valley flight legs in 8-11 levels of elevation. The grey line is the contour of zero along-valley velocity. Note the different grey scale on 25 August.

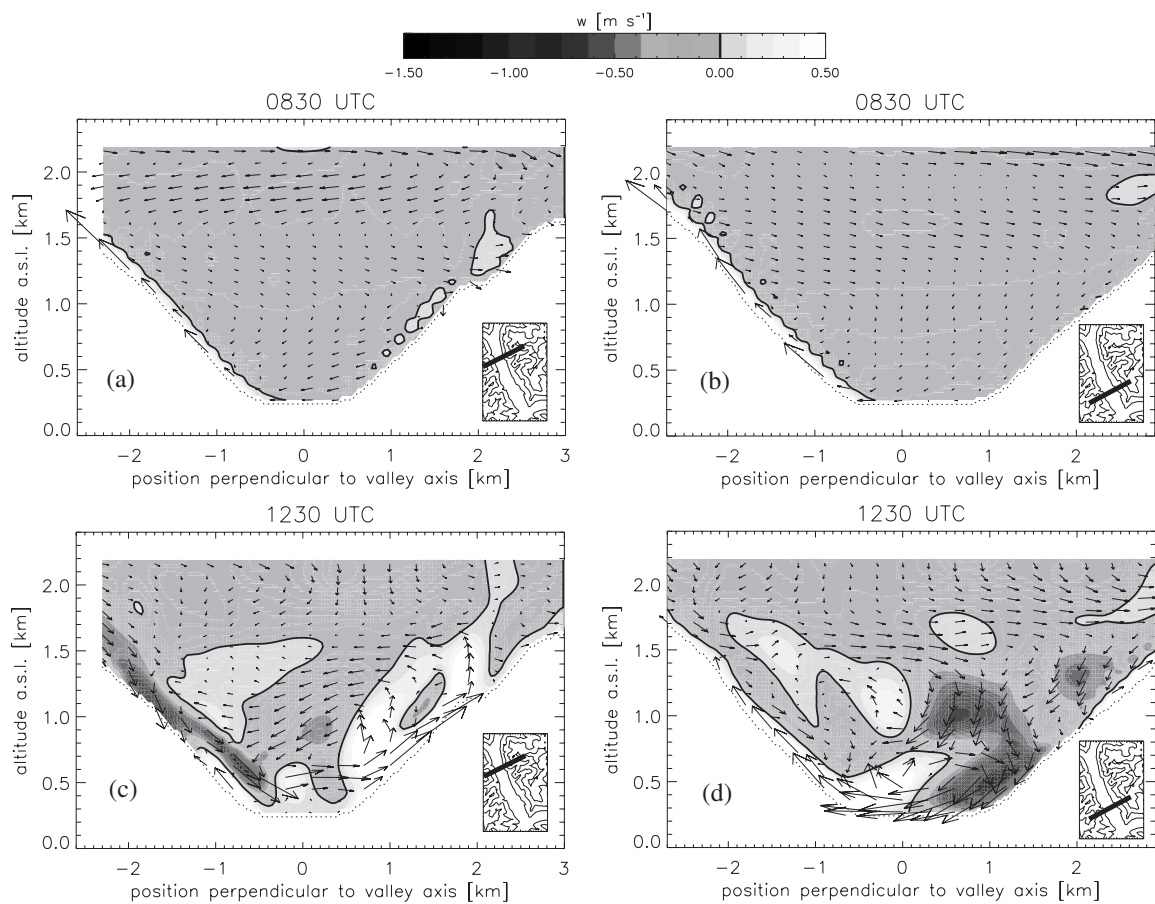


Figure 6: Simulated cross-valley wind vectors on 22 August in two slices across the Riviera Valley (as indicated on the small topography panels): one in the northern half of the valley (a,c), and one close to the southern valley mouth (b,d). The upper panels show the cross-valley flow at 0830 UTC, the lower ones at 1230 UTC. The shading indicates vertical wind velocity. The black line is the contour of zero vertical velocity.

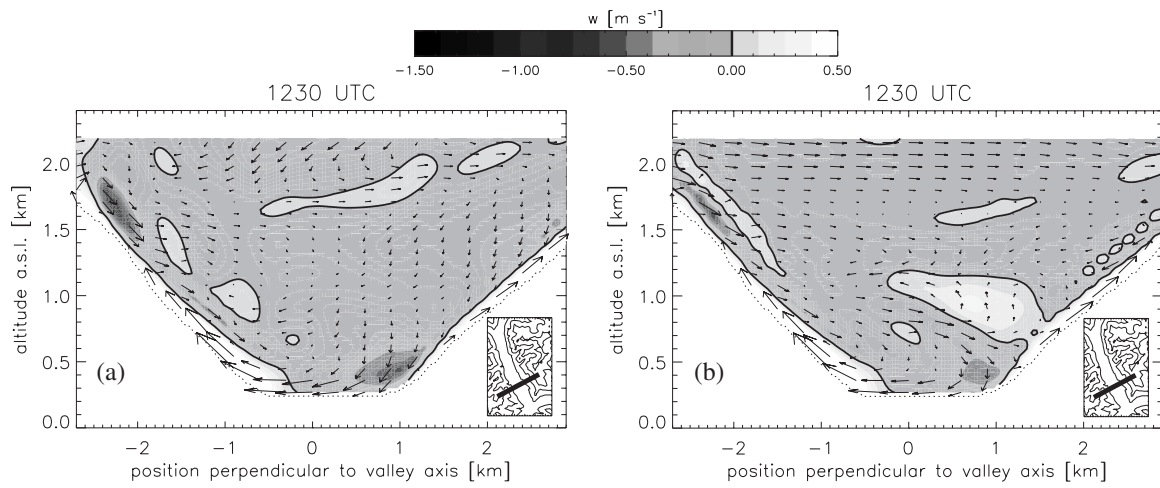


Figure 7: Simulated cross-valley wind vectors in a slice close to the southern valley mouth on 21 August (a) and 25 August (b) at 1230 UTC. The shades of grey indicate vertical wind velocity. The black line is the contour of zero vertical velocity.

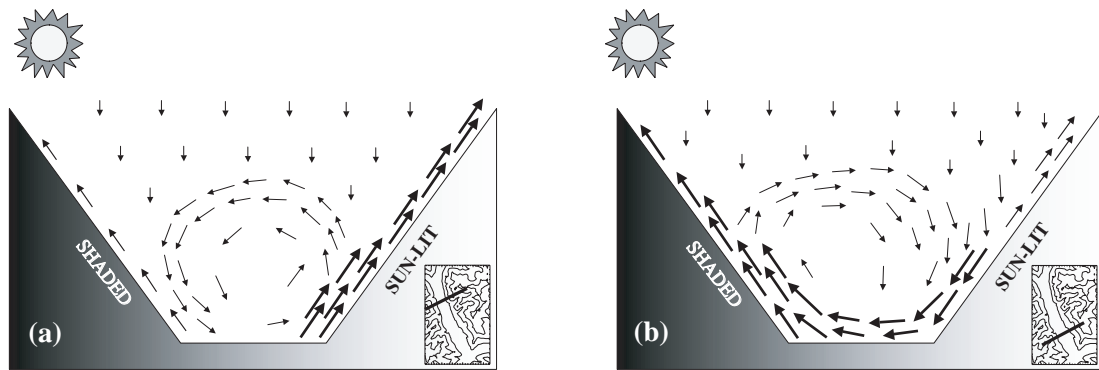


Figure 8: Schematic representation of the afternoon cross-valley flow in two cross-sections in the Riviera Valley (as indicated in the small topography-panels). (a) shows the thermally driven counter-clockwise circulation observed in the northern half of the valley, while (b) displays the curvature-induced clockwise secondary circulation of the southern valley entrance region.

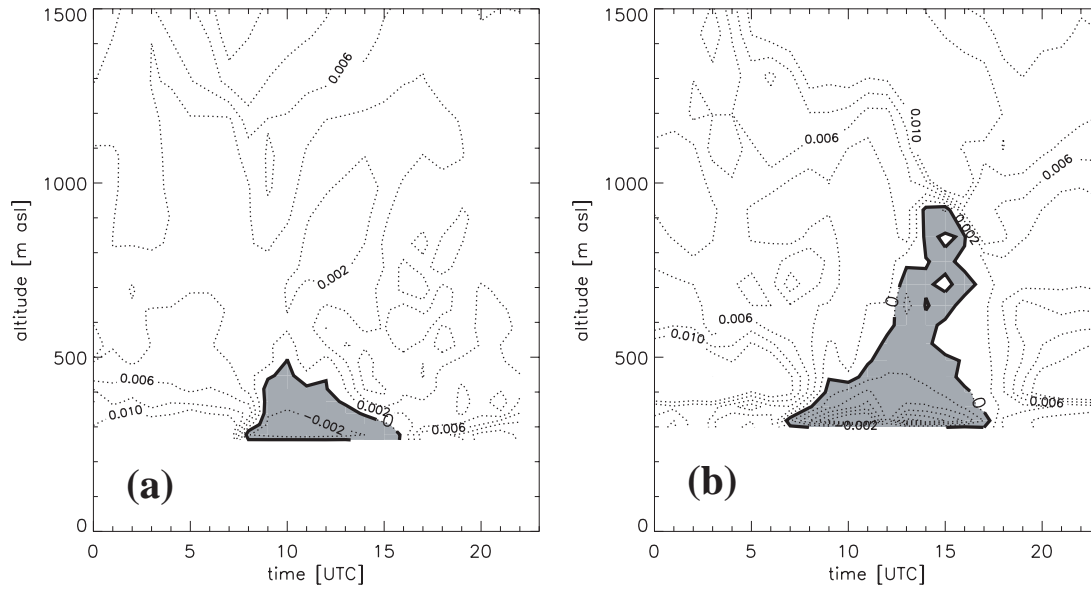
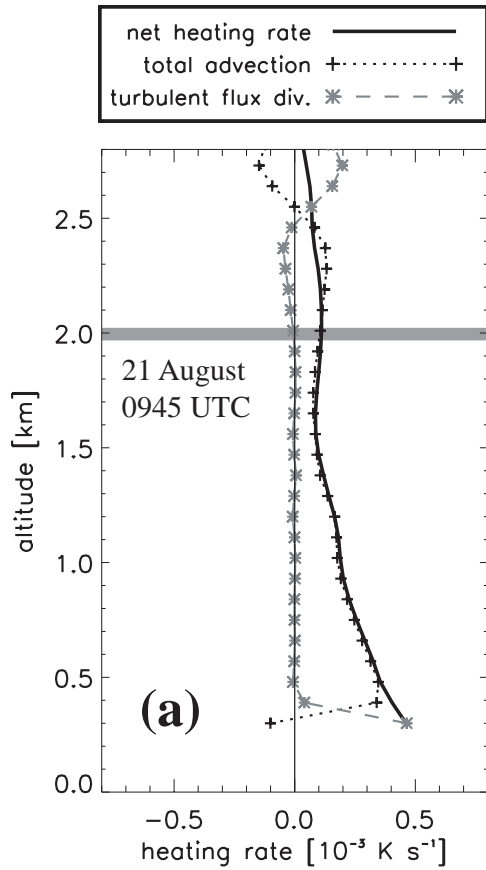


Figure 9: Time-height plots of simulated vertical gradients of potential temperature on 25 August (contours labeled in $K m^{-1}$). The shading indicates neutral to super-adiabatic stratification. (a) is in the Riviera Valley (at site A1) and (b) at a location approximately 50 km southwest of the Riviera Valley ($45.93^{\circ}N$, $8.77^{\circ}E$), i.e. at the beginning of the foothills of the Alps (obtained from the 1 km grid).

S150: HEAT BUDGET



S150: ADVECTION

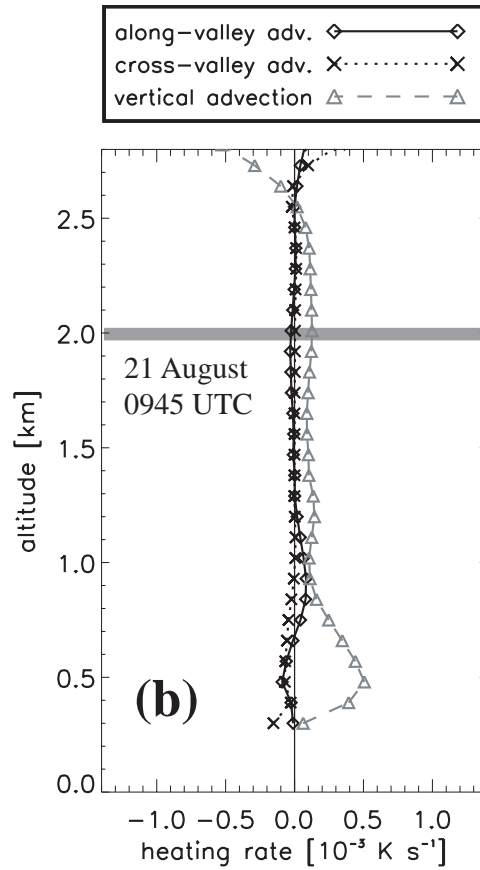


Figure 10: Simulated profiles of (a) the heat budget contributions and (b) the respective advection terms in the valley coordinate system on the **late morning** of 21 August. The profiles are 90-minute averages (centered at 0945 UTC) over the valley base width in slice **S150** (see Fig. 1b). The grey bar indicates the crest height.

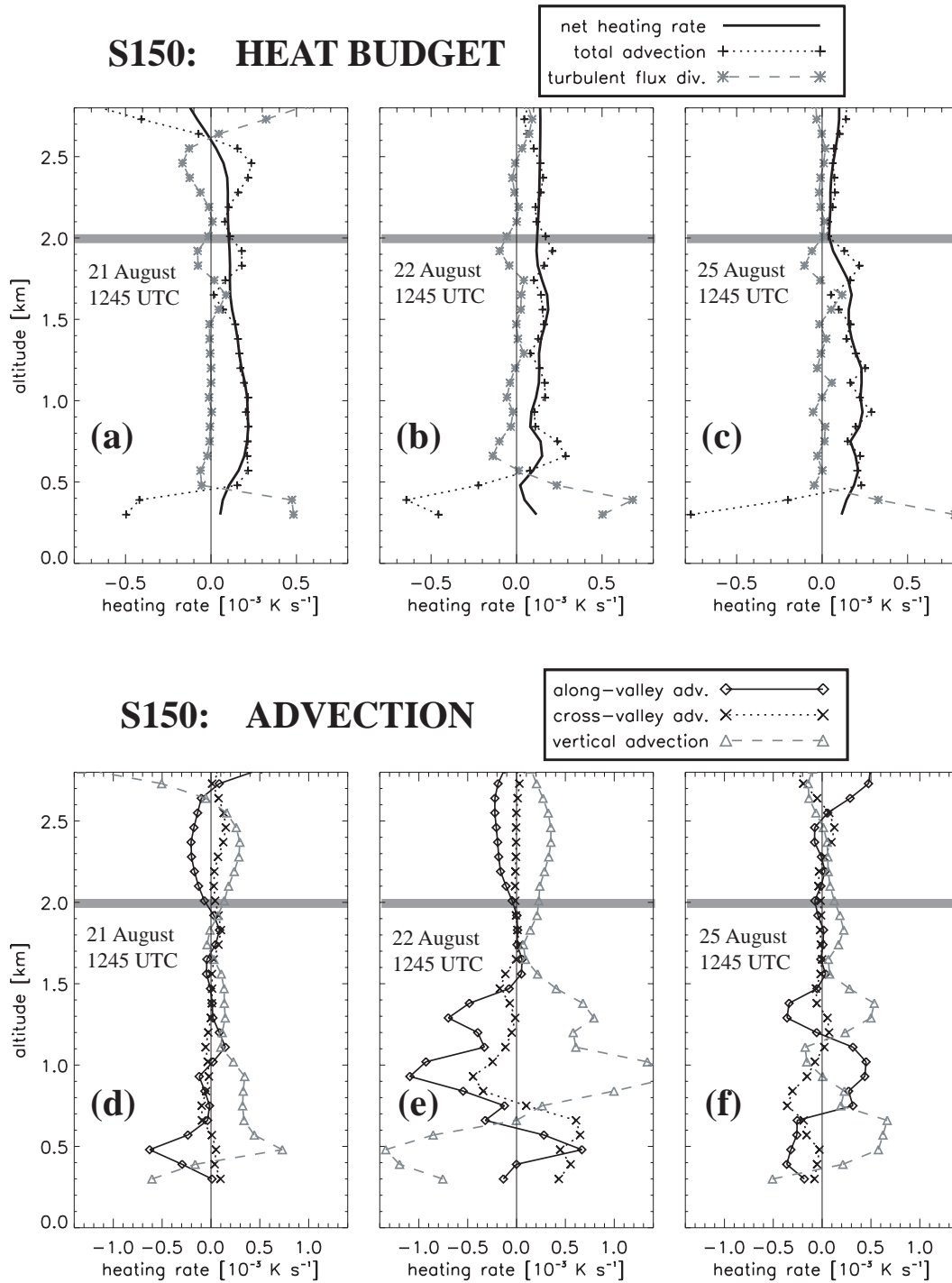
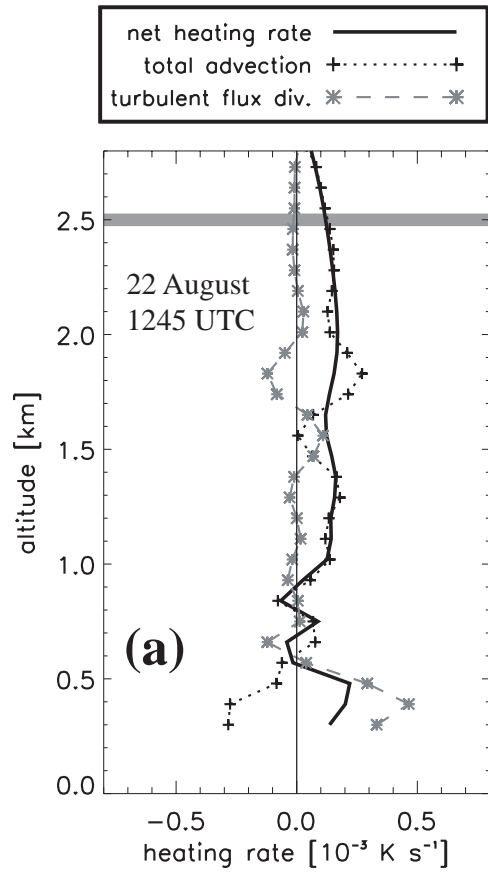


Figure 11: Simulated profiles of the heat budget contributions (upper row) and the respective advection terms in the valley coordinate system (lower row) on the **afternoons** of 21 August (a,d), 22 August (b,e) and 25 August (c,f). The profiles are 90-minute averages (centered at 1245) over the valley base width in slice **S150** (see Fig. 1b). The grey bar indicates the crest height.

N150: HEAT BUDGET



N150: ADVECTION

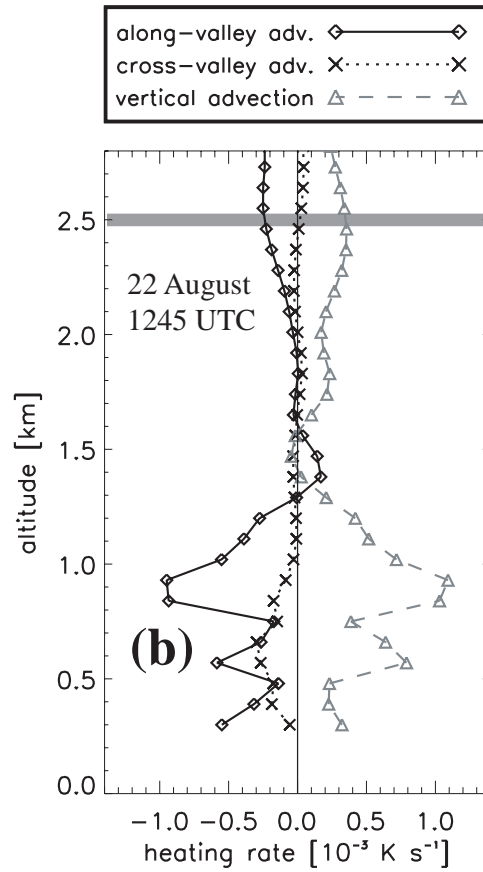


Figure 12: Simulated profiles of the heat budget contributions (a) and the respective advection terms in the valley coordinate system (b) on the **afternoon** of 22 August. The profiles are 90-minutes averages (centered at 1245 UTC) over the valley base width in slice **N150** (see Fig. 1b). The grey bar indicates the crest height.

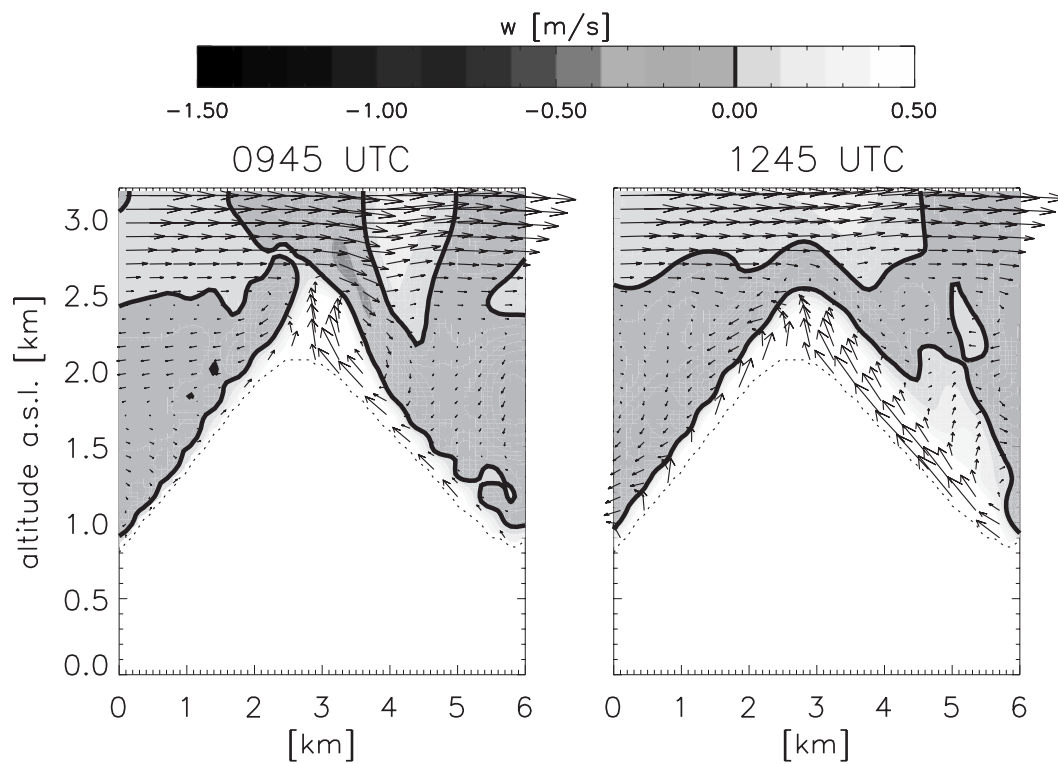


Figure 13: Simulated flow structure in a vertical slice across the ridge east of surface station A1, showing the venting of boundary layer air into the free atmosphere on 21 August at (a) 0945 UTC and (b) 1245 UTC. The contours indicate vertical wind velocity, with the black line being zero vertical velocity.

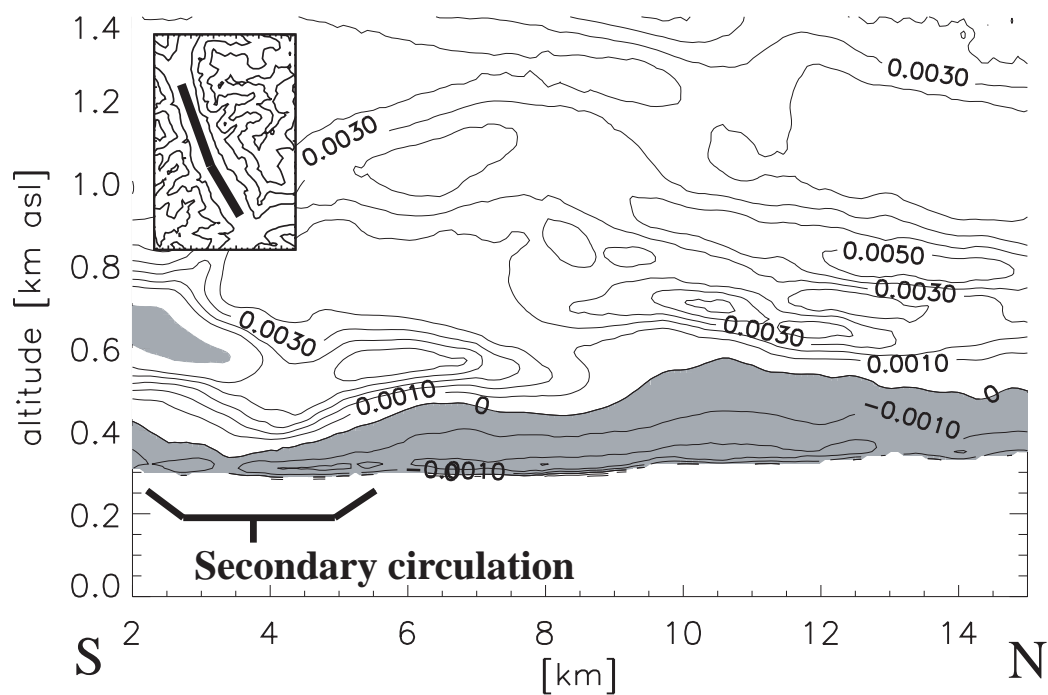


Figure 14: Variation of well-mixed layer thickness in the along-valley direction on 22 August at 1245 UTC as simulated with ARPS. The contours (labeled in $K m^{-1}$) show the vertical gradient of potential temperature, with areas of neutral or super-adiabatic stratification being shaded in grey. The position of the secondary circulation is indicated. Along-valley distance has an arbitrary origin at the town of Bellinzona (Fig. 1).

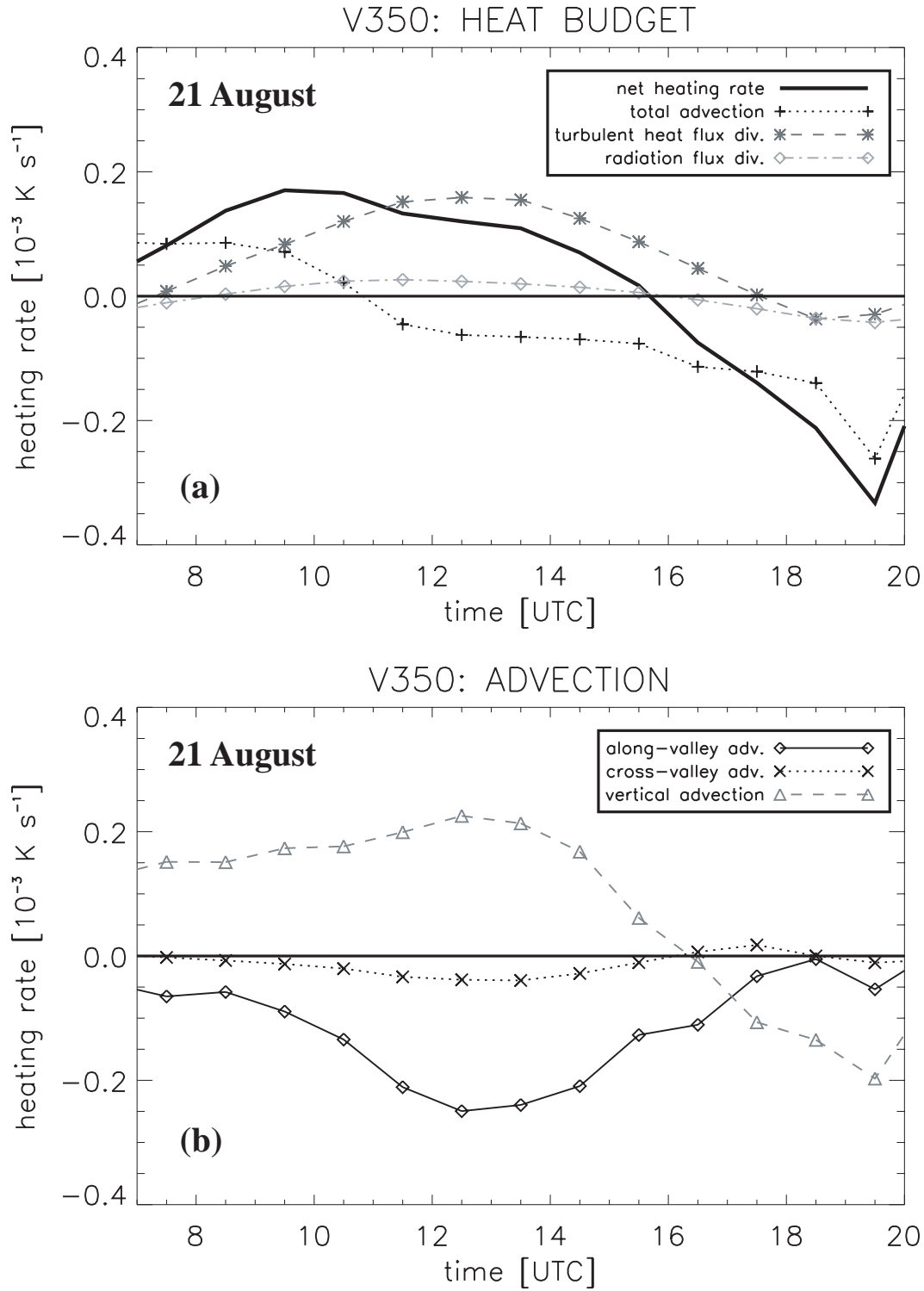


Figure 15: Time-series from simulations of (a) the heat budget components and (b) the advection components on 21 August, averaged over V350 on the 350 m grid (see Fig. 1b).

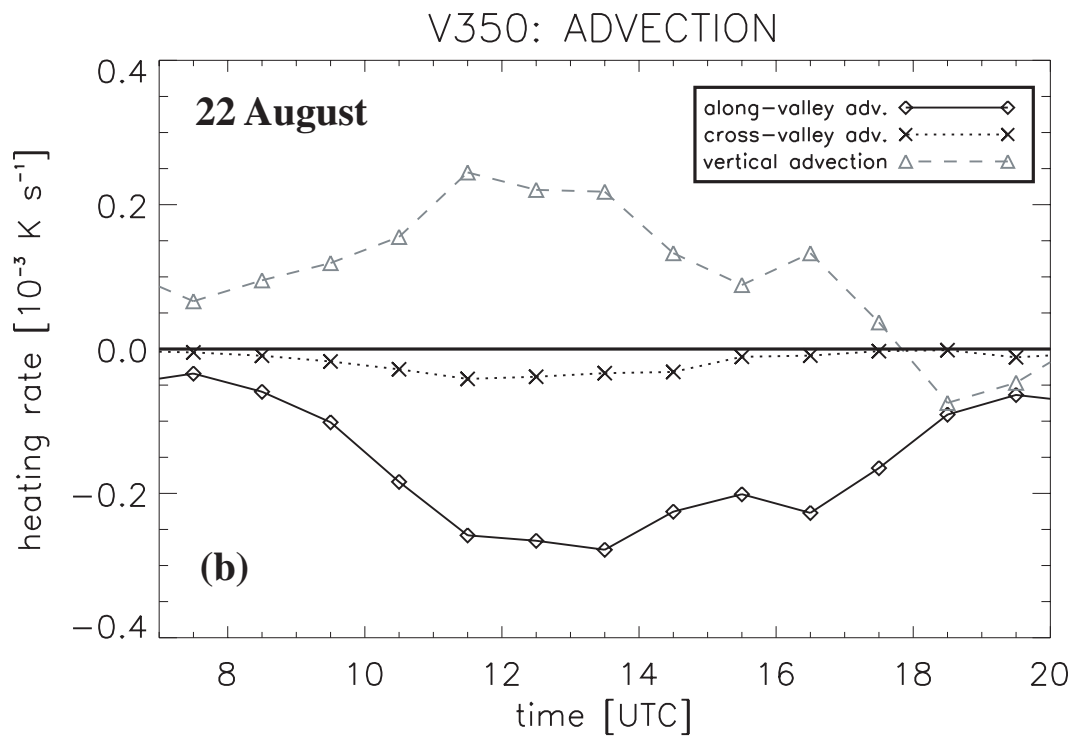
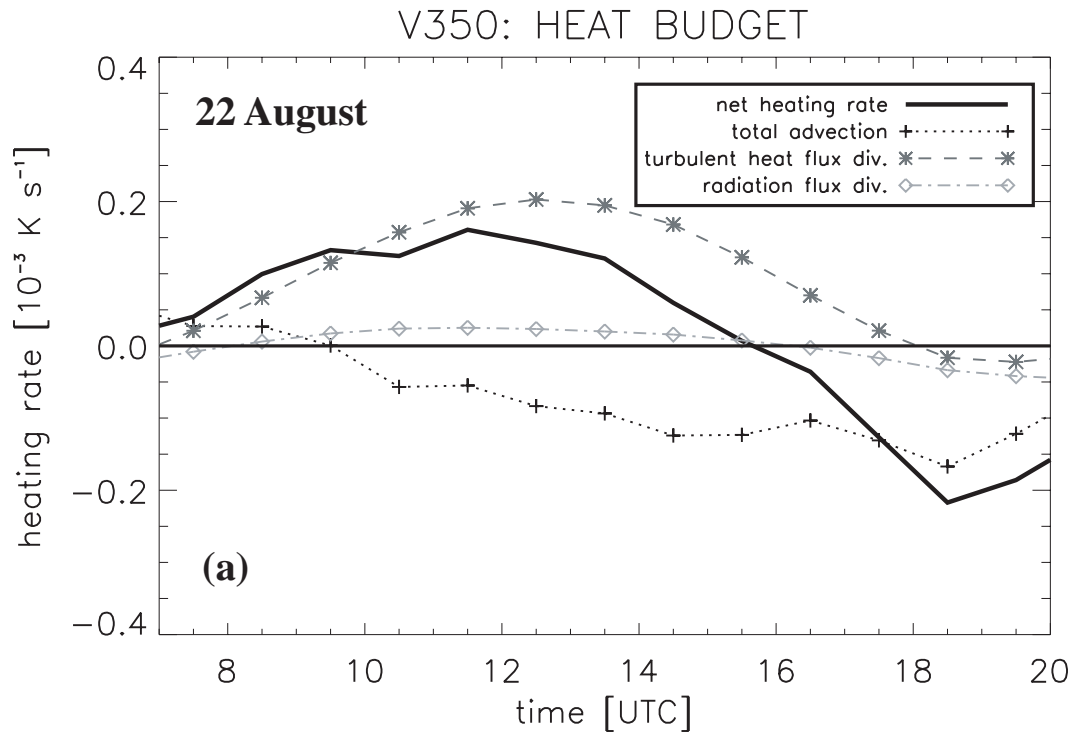


Figure 16: As Fig. 15, but for 22 August.

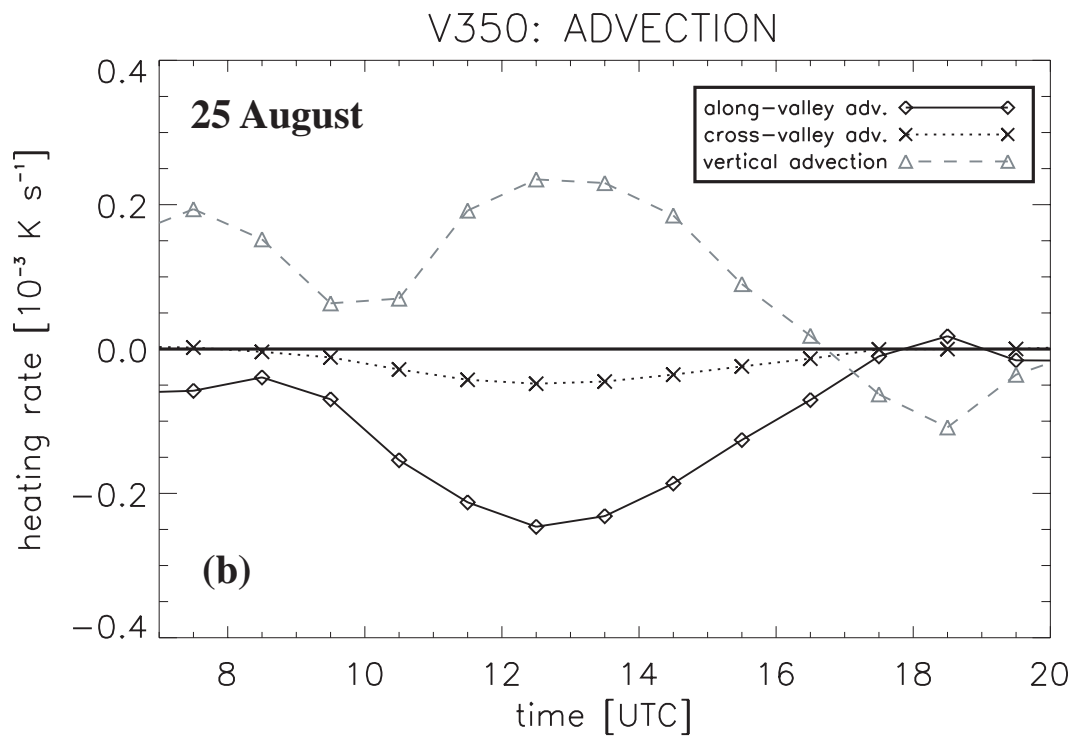
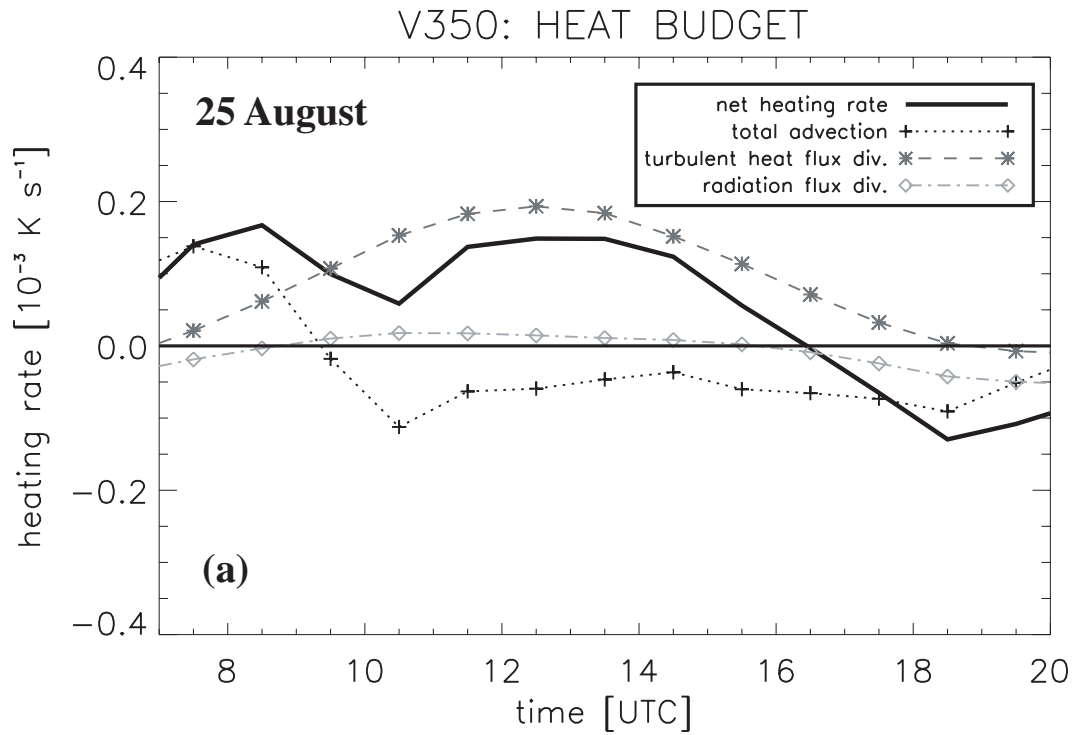


Figure 17: As Fig. 15, but for 25 August.